atmosphere

MDPI

Article

Stable Boundary Layers and Subfilter-Scale Motions

James C. McWilliams [1], Charles Meneveau [2], Edward G. Patton [3] and Peter P. Sullivan [3,*]

[1] Department of Atmospheric and Oceanic Sciences, University of California, Los Angeles, CA 90095, USA; jcm@atmos.ucla.edu
[2] Department of Mechanical Engineering, Johns Hopkins University, Baltimore, MD 21218, USA; meneveau@jhu.edu
[3] National Center for Atmospheric Research, Boulder, CO 80301, USA; patton@ucar.edu
* Correspondence: pps@ucar.edu

Abstract: Recent high-resolution large-eddy simulations (LES) of a stable atmospheric boundary layer (SBL) with mesh sizes $N = (512^3, 1024^3, 2048^3)$ or mesh spacings $\triangle = (0.78, 0.39, 0.2)$ m are analyzed. The LES solutions are judged to be converged based on the good collapse of vertical profiles of mean winds, temperature, and low-order turbulence moments, i.e., fluxes and variances, with increasing N. The largest discrepancy is in the stably stratified region above the low-level jet. Subfilter-scale (SFS) motions are extracted from the LES with $N = 2048^3$ and are compared to sonic anemometer fields from the horizontal array turbulence study (HATS) and its sequel over the ocean (OHATS). The results from the simulation and observations are compared using the dimensionless resolution ratio $\Lambda_w/\triangle_f$ where $\triangle_f$ is the filter width and Λ_w is a characteristic scale of the energy-containing eddies in vertical velocity. The SFS motions from the observations and LES span the ranges $0.1 < \Lambda_w/\triangle_f < 20$ and are in good agreement. The small, medium, and large range of $\Lambda_w/\triangle_f$ correspond to Reynolds-averaged Navier–Stokes (RANS), the gray zone (a.k.a. "Terra Incognita"), and fine-resolution LES. The gray zone cuts across the peak in the energy spectrum and then flux parameterizations need to be adaptive and account for partially resolved flux but also "stochastic" flux fluctuations that represent the turbulent correlation between the fluctuating rate of strain and SFS flux tensors. LES data with mesh 2048^3 will be made available to the research community through the web and tools provided by the Johns Hopkins University Turbulence Database.

Keywords: stratified turbulence; large-eddy simulation; subfilter-scale motions; surface layer observations; gray zone

Citation: McWilliams, J.C.; Meneveau, C.; Patton, E.G.; Sullivan, P.P. Stable Boundary Layers and Subfilter-Scale Motions. *Atmosphere* **2023**, *14*, 1107. https://doi.org/10.3390/atmos14071107

Academic Editor: Stephan De Wekker

Received: 20 April 2023
Revised: 15 May 2023
Accepted: 19 May 2023
Published: 4 July 2023

1. Preface

Along with others in this collection, this paper is dedicated to our colleague and friend, Jack(son) Herring. It is also an encomium for the long history of turbulence research centered around the National Center for Atmospheric Research (NCAR), where Jack worked from 1972. One of the better purposes of NCAR was as a gathering place for researchers from around the world, especially in the summer outside of teaching terms. Another was as a national supercomputing center beginning even before such a term was invented (i.e., punch cards in the basement of the Mesa Laboratory), and from the outset turbulence simulations were one of the premier scientific applications [1]. The summer gatherings were often informal and barely scripted or sometimes formally funded and convened as workshops. They did a great deal to fertilize the development of turbulence theories, simulations, and experiments among the physics, engineering, and geophysical fluid dynamics communities and to entrain younger scientists into the subject. A conspicuous event was a summer-long school and symposium in 1987 [2]. It was partly managed under the auspices of NCAR's Advanced Study Program, where Jack was first hired, and at some point in the 1980s it was more formally designated as the Geophysical Turbulence Program (GTP) that continues today. Its scientific scope was broad and its human reach

was wide, involving hundreds of scientists whose roster probably no archaeology could recover. Among its luminaries from outside NCAR were R. Kraichnan, U. Frisch, E. Lorenz, D. Montgomery, H. Tennekes, M. Lesieur, and J. Riley, and from within, C. Leith, D. Lilly, J. Deardorff, J. Wyngaard, D. Lenschow, and A. Pouquet; there were many others in and outside NCAR, ourselves, and of course Jack.

2. Introduction

Stratified turbulence impacts many applications and the topic attracts researchers in the physics, geophysical, and engineering communities; see reviews [3–6]. The present contribution is narrower in scope, focusing on stably stratified turbulent boundary layers (SBLs). The SBL is a key component of earth-system modeling, viz., large-scale weather, climate, and ocean models [4,5,7–12]. Stratified boundary-layer turbulence is also important in electromagnetic wave propagation in the lower atmosphere, wind energy, and the dispersion of pollutants [13–15].

Observations, along with direct numerical simulation (DNS) and large-eddy simulation (LES), are important tools for studying SBLs, but each face impediments; simulation results are often at low Reynolds number [16] and require long computational run times, and observations are impacted by inherent atmospheric variability and surface heterogeneity; the latter can result in global impacts on the SBL [17]. Observations and simulations must cope with spatial and temporal intermittency in SBLs with strong stratification [5] and coherent structures [18].

This paper is a report of recent, very-high-resolution simulations of stable atmospheric boundary layers (SBL) underneath a steady geostrophic wind. It is one of the canonical idealized problems in geophysical fluid dynamics, closely related to Jack's interest in homogeneous stratified turbulence, but with the complication of an adjacent rough, flat boundary. The narrow purpose here is to report on the resolution dependency in LES and make detailed statistical comparisons with near-surface measurements from instrument arrays. A larger goal is to establish the validity of SBL LES as a test-bed for evaluating turbulent closure schemes near the boundary, although we have not yet gone very far in that direction.

The outline of the rest of the paper is the following: Section 3 presents the LES equations and introduces recent LES of SBLs with fine-mesh resolution; Section 4 briefly describes field observations collected in the atmospheric surface layer specifically designed to measure subfilter-scale (SFS) fields over a range of atmospheric stability; Section 5 analyzes the LES solutions and their sensitivity to the mesh resolution and compares SFS motions extracted from the LES and field observations; Section 6 summarizes the findings; and Section 7 is a brief commentary on the continuing science of turbulence.

3. LES

3.1. Governing Equations

The LES model equations for an SBL under the Boussinesq approximation with system rotation and stable stratification with a flat bottom boundary are well documented [19,20]. The equations are briefly introduced here:

$$\frac{\partial \overline{\mathbf{u}}}{\partial t} + \overline{\mathbf{u}} \cdot \nabla \overline{\mathbf{u}} = -\mathbf{f} \times (\overline{\mathbf{u}} - \mathbf{U}_g) - \nabla \overline{\pi} + \hat{\mathbf{z}} \beta (\overline{\theta} - \theta_{ref}) - \nabla \cdot \mathbf{T} \tag{1a}$$

$$\frac{\partial \overline{\theta}}{\partial t} + \overline{\mathbf{u}} \cdot \nabla \overline{\theta} = -\nabla \cdot \mathbf{B} \tag{1b}$$

$$\frac{\partial e}{\partial t} + \overline{\mathbf{u}} \cdot \nabla e = \mathcal{P} + \mathcal{B} + \mathcal{D} - \mathcal{E} \tag{1c}$$

$$\nabla \cdot \overline{\mathbf{u}} = 0 \,. \tag{1d}$$

The equation set includes transport equations: for momentum $\rho \overline{\mathbf{u}}$ (1a); for virtual potential temperature $\overline{\theta}$ (1b); and for SFS turbulent kinetic energy e (1c). The divergence-free

(incompressible) condition (1d) determines the elliptic pressure variable $\overline{\pi}$. The variables that appear in (1) are: velocity components $\overline{\mathbf{u}} \equiv \overline{u}_i = (\overline{u}, \overline{v}, \overline{w})$, geostrophic winds $\mathbf{U}_g = (U_g, V_g)$, rotation vector $\mathbf{f} = (0, 0, f)$ with Coriolis parameter f, unit vector $\hat{\mathbf{z}}$ in the vertical direction, and buoyancy parameter $\beta = g/\theta_{ref}$, where g is gravity and θ_{ref} is a reference temperature. Pressure $\overline{p}$ and air density ρ do not appear explicitly in (1). The terms on the right-hand side of (1c) for e are shear production $\mathcal{P}$, buoyancy production–destruction $\mathcal{B}$, diffusion $\mathcal{D}$, and dissipation $\mathcal{E}$. The modeling of these terms is described in [19]. The overbar notation $\overline{(\,)}$ denotes a spatially filtered quantity.

The LES equations are formally derived by applying a spatial filter term-by-term to the governing equations of motion, although physics-inspired alternatives are possible [21]. This operation introduces the unknown SFS kinematic momentum and temperature fluxes

$$\mathbf{T} \equiv \tau_{ij} = \overline{u_i u_j} - \overline{u}_i \overline{u}_j \quad ; \quad \mathbf{B} \equiv \tau_{i\theta} = \overline{u_i \theta} - \overline{u}_i \overline{\theta} \tag{2}$$

For the SBL we adopt the two-part SFS model proposed by Sullivan et al. [22], which utilizes the transport Equation (1c) and an eddy viscosity approach in the parameterization of the SFS fluxes given by (2). This parameterization is specifically tailored to a high-Reynolds-number LES that uses rough-wall surface boundary conditions based on Monin–Obukhov (MO) similarity theory. In the eddy viscosity prescription $\nu_t \sim \gamma \sqrt{e}\, \ell$ the isotropy factor $\gamma = S'/(\langle S \rangle + S')$ where $(\langle S \rangle, S')$ are the resolved strain rate average and fluctuation, respectively; the strain rate average is over an x–y plane. The isotropy factor varies with the grid resolution and essentially reduces the length scale ℓ as the wall is approached depending on the magnitude of the resolved turbulence fluctuations. The boundary conditions, solution algorithm, and further details are provided in Sullivan et al. [20]. To streamline the notation and text in the following discussion, we now drop the overbar symbol on all spatially filtered (i.e., resolved) variables and simply refer to the virtual potential temperature θ as "temperature".

3.2. LES of Stable Boundary Layers

The present work targets the LES of the so-called GABLS1 intercomparison case described in detail by Holtslag [23] and Beare et al. [24]. The problem design provides an excellent test-bed to study stratified turbulence in a high-Reynolds-number boundary-layer flow using LES. GABLS1 is a canonical high-latitude SBL driven by constant geostrophic winds $U_g = 8$ m s^{-1} with Coriolis parameter $f = 1.39 \times 10^{-4}$ s^{-1} above a horizontally homogeneous rough surface $z_o = 0.1$ m. The simulations are initiated from a neutral state with an overlying stable inversion $\partial_z \theta = 0.01$ K m^{-1} imposed at an initial height $z = 100$ m. The computational domain size is $(400 \times 400 \times 400)$ m. A constant rate of surface cooling $C_r = 0.25$ K h^{-1} is applied starting at $t = 0$ to generate stably stratified turbulence. The specification of surface temperature fully couples the momentum and temperature relations in the Monin–Obukhov bottom boundary conditions, which is a more demanding test for LES compared to a specified temperature flux: further description of the simulation design is given in Sullivan et al. [20]. Previous LESs find a quasi-steady SBL featuring a low-level jet with wind profile veering in the SBL after 8 h of simulation; the SBL depth $h \approx 200$ m, the surface temperature flux $Q_* \approx -9$ K m s^{-1}, and friction velocity $u_* \approx 0.25$ m s^{-1}, which vary with the mesh resolution [20]. The GABLS1 SBL is weakly stable with continuous turbulence and the boundary-layer stability metric is $h/L_{mo} \sim 1.7$, where $L_{mo} \approx 118$ m is the Monin–Obukhov length; see Table 1 and definitions of h, L_{mo} in Section 5.1.

The first GABLS1 intercomparison used LES models with coarse and fine meshes of $N = 128^3$ and 200^3 gridpoints [24,25], suitable for the computational capabilities at that time. Although there was qualitative agreement amongst the LES models, there are hints that an increased resolution resulted in shallower SBLs inducing a change in the surface friction velocity u_* and surface cooling flux Q_*. This motivated further study and Sullivan et al. [20] explored the LES solution sensitivity using meshes of $N = (200^3, 512^3, 1024^3)$ gridpoints along with four different cooling rates $C_r = (0.25, 0.375, 0.5, 1.0)$ K h^{-1}; the 1024^3 simulation required approximately 2 million core hours to complete a 9 h simulation.

Table 1. Bulk simulation properties, with entries: LES case, mesh points N, cooling rate C_r, mesh spacing $\triangle$, friction velocity u_*, temperature flux Q_*, boundary-layer height h, Monin–Obukhov stability length L_{mo}, boundary-layer stability h/L_{mo}.

Case	N	C_r (K h^{-1})	$\triangle$ (m)	u_* (m s^{-1})	$Q_* \times 10^3$ (K m s^{-1})	h (m)	L_{mo} (m)	h/L_{mo}
B	512^3	0.25	0.78	0.265	−10.5	205.3	119.3	1.72
C	1024^3	0.25	0.39	0.255	−9.63	197.5	116.4	1.70
C2	2048^3	0.25	0.20	0.249	−8.83	187.2	118.6	1.56
F2	2048^3	1.0	0.20	0.177	−14.82	143.7	24.9	5.77

The present work expands on Sullivan et al. [20] using an unprecedented resolution of $\triangle = 0.2$ m in all three directions with a mesh of $N = 2048^3$. Because of the computational cost a two-step recipe is used to perform the LES. First, a seed simulation with $N = (512 \times 512 \times 2048)$ is run from scratch for nearly 8 h. The grid in this simulation is anisotropic but has the advantage that the wind and temperature profiles vary smoothly in the vertical direction. Next, the last volume from the seed simulation is archived and the field variables are interpolated in the horizontal x–y directions using zero-padded Fourier transforms to generate a restart volume with $N = 2048^3$ points. The fine-mesh solution is then started and run for an additional 0.5 h. This simulation strategy results in smooth restarts with the high-wavenumber part of the spectrum rapidly filled with small-scale turbulence. Two simulations with weak and strong cooling rates $C_r = (0.25, 1)$ K h^{-1} are carried out.

Selected snapshots from the two simulations as well as time sequences with the 2048^3 mesh are being included as part of datasets available to the community at the Johns Hopkins Turbulence Databases (JHTDB). The system enables scientists' access to world-class simulations using the approach of "Immersive Analysis", which allows the user to insert immersive "virtual sensors" into the simulated flow. This approach facilitates access to large datasets without having to download large amounts of data, as well as performing analysis close to the data [26,27]. The ability to query the data in a spatially localized fashion is particularly relevant to the SBL, whose fields are characterized by strong spatially and temporally intermittent events. At the time of this writing, the data ingestion and data publishing process has not yet been finished, but completion is expected soon.

4. Observations of Subfilter-Scale Motions

An alternative to using low-Reynolds-number DNS datasets for a priori tests [28] of SFS models is to use laboratory measurements of higher-Reynolds-number turbulence collected at multiple spatial points. In principle, the measurement data can then be spatially filtered, mimicking the spatial-filtering operation in LES [29]. At still-higher Reynolds numbers a similar approach can be undertaken using measurements in the atmospheric surface layer. The latter was frequently championed in seminars and discussions with John Wyngaard when visiting NCAR. The horizontal array turbulence study (HATS) was a field campaign [30] specifically designed to construct SFS motions from turbulence data collected at multiple locations in the atmospheric surface layer over a range of stability. HATS, carried out in the central California valley, was a collaborative community effort between NCAR, GTP, Johns Hopkins University, Pennsylvania State University, and Clemson University. The field campaign built on work by several groups, including Meneveau and Lund [31], Tong et al. [32,33], Tao et al. [34]; see the many cited references in these papers and the review [35].

HATS used two horizontal crosswind arrays of sonic anemometers mounted at different vertical locations, as shown in Figure 1; four array configurations varying the sonic anemometer horizontal separation and vertical location were used in HATS. The anemometer arrays measured time series of the turbulent velocity components (u, v, w) (streamwise, crosswind, and vertical, respectively) and virtual potential temperature θ. The multi-point measurements in the crosswind direction y are combined with Taylor's frozen-field assumption in the streamwise direction x [36] to create x–y planes of stratified

turbulence $(\mathbf{u}, \theta)(x, y, z, t)$. The wind speed and diurnal variations combined with spatial variations in the instrument positioning created a rich dataset for studying spatially filtered turbulence in the atmospheric surface layer. For example, Sullivan et al. [37], Kleissl et al. [38,39], Wyngaard [40], Chen and Tong [41], Hatlee and Wyngaard [42], Chamecki et al. [43] and Ramachandran and Wyngaard [44] studied SFS dynamics and evaluated eddy viscosity models, dynamic Smagorinsky models, subfilter-scale budgets, and rate-equation models using HATS data; the studies employed single and double filtering available from the HATS arrays. Triple filtering was explored in Higgins et al. [45] using a 4×4 array of sonic anemometers that also enabled vertical (albeit more sparsely sampled) filtering, confirming the accuracy of double filtering. Kumar et al. [46] reproduced HATS conditions during a daily cycle using low-resolution LES. The success of HATS motivated follow-on campaigns focused on atmospheric turbulence in the surface layer; over the ocean OHATS [47], over a glacier SnoHATS [48], in an orchard canopy CHATS [49], and over land accounting for horizontal advection AHATS [50].

Figure 1. Twin horizontal arrays of sonic anemometers used to measure subfilter-scale variables in the atmospheric surface in the HATS field campaign. The upper array is located at $z_d = 8.66$ m with anemometer horizontal spacing $\delta y_d = 2.17$ m. The vertical location and horizontal spacing of anemometers in the lower array are $(z_s, \delta y_s) = (4.33, 1.08)$ m. Photo courtesy of Thomas Horst (NCAR).

5. Results

5.1. SBL Low-Order Moments

The advent of high-performance computing allows mesh convergence to be studied using 3D simulations. Solution convergence in LES is complicated by the mesh dependence in the SFS model, e.g., holding the domain size fixed, the resolved flux in a 100^3 simulation is of course different than the resolved flux in a 2048^3 simulation. Judging convergence in LES is also challenging as the subgrid-scale model and numerical discretization errors are intertwined since both depend explicitly on the mesh spacing [51]. Here we use physically based metrics based on the vertical profiles of low-order statistical moments to judge convergence, as discussed in Sullivan and Patton [52] for convectively driven boundary layers; also see Geurts and Fröhlich [53]. Table 1 provides a summary of the bulk parameters for SBL simulations with $C_r = 0.25$ K h^{-1}, grid meshes $N = (512^3, 1024^3, 2048^3)$,

$C_r = 1$ K h^{-1}, $N = 2048^3$. The variables in Table 1 are the LES case, grid mesh points N, mesh spacing $\triangle$, cooling rate C_r, friction velocity u_*, surface temperature flux Q_*, boundary-layer depth h, Monin–Obukhov stability length $L_{mo} = -u_*^3/\kappa\beta Q_*$ with von Kármán constant $\kappa = 0.4$, and boundary-layer stability h/L_{mo}. The SBL depth h is defined as the vertical location where the vertical gradient of temperature $\partial_z\langle\theta\rangle$ reaches a maximum (see [20,54]). There is variation in (u_*, Q_*) with the grid resolution because of variability in the SBL depth h. Dai et al. [55] speculates that this is a consequence of the stability length-scale correction used in the LES. Statistics, denoted by angle brackets $\langle\ \rangle$, are formed by averaging in the x–y planes and over the time period $8 < t < 9$ h, except for simulation C2, which used a shorter 30 min time average. A turbulent fluctuation from a horizontal mean is denoted by a superscript prime $(\ )'$.

Figure 2 compares the profiles of winds and temperature for three different resolutions $(512^3, 1024^3, 2048^3)$ with fixed surface cooling $C_r = 0.25$ K h^{-1}. To eliminate the slight variability with the boundary-layer depth we introduce the dimensionless vertical coordinate z/h, as shown in the right panel of Figure 2. The flux and variance profiles are normalized by the surface values (u_*^2, Q_*) as appropriate. Under this normalization the wind profiles collapse well (the right panel of Figure 2). The low-level jet is positioned at $z/h = 0.8$ and its magnitude is 1.2 U_g.

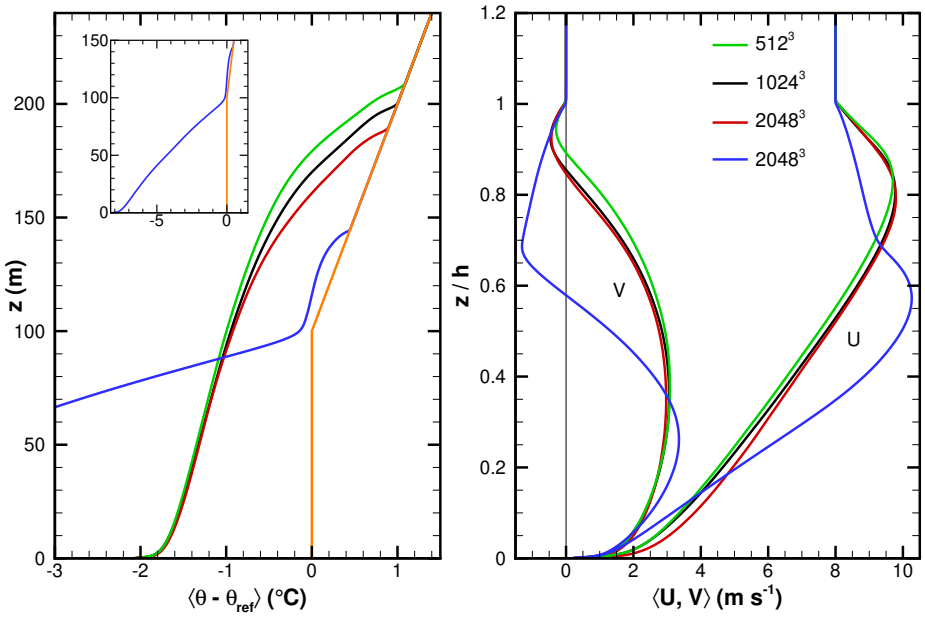

Figure 2. Vertical profiles of average temperature $\langle\theta - \theta_{ref}\rangle$ (**left panel**). Simulations (B, C, C2) with cooling rate $C_r = 0.25$ K h^{-1} and $N = (512^3, 1024^3, 2048^3)$ are represented by line colors (green, black, red), respectively. Simulation F2 with $C_r = 1$ K h^{-1} and $N = 2048^3$ is presented in blue. The inset figure shows the variation of temperature in F2 in the lower SBL. The initial temperature field at $t = 0$ is shown as the orange line and $\theta_{ref} = 265$ K. Vertical profiles of average winds $\langle U, V\rangle$ are shown in the **right panel**. Note that the vertical coordinate for the wind profiles is normalized by the SBL height h from each simulation.

The vertical profiles of the Richardson number Ri and the squared shear and buoyancy frequency (S^2, N^2) are displayed in Figure 3 for the three resolutions considered. Here

$$Ri(z) = \frac{N^2}{S^2} \ ; \ N^2 = \frac{g}{\theta_{ref}}\frac{\partial\langle\theta\rangle}{\partial z} \ ; \ S^2 = \left(\frac{\partial\langle\mathbf{u}_\perp\rangle}{\partial z}\right)^2. \tag{3}$$

where the horizontal wind aligned with the mean wind direction is given by $u_h = \mathbf{u}_\perp(\mathbf{x}, t) \cdot \langle\mathbf{u}_\perp\rangle/|\langle\mathbf{u}_\perp\rangle|$. The profiles of (Ri, S^2, N^2) are very well converged for the three different

mesh resolutions below $z/h < 0.5$. In the upper SBL, above the low-level jet the profiles for simulations C2 and C are converged. These profiles show that the simulation is in the weakly stable regime as in Sullivan et al. [20]. In particular, the profile $Ri(z) \approx 0.2$ shows the approximate validity of the very simple RANS parameterization of a constant Richardson number above the Monin–Obukhov surface layer.

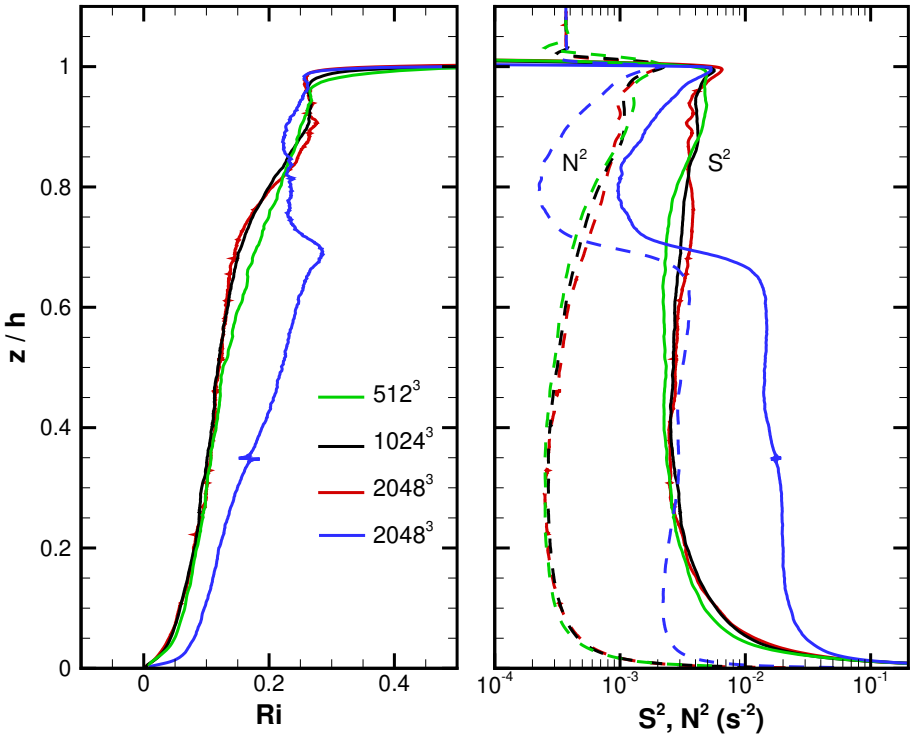

Figure 3. Vertical profiles of average Richardson number (**left panel**). Simulations with cooling rate $C_r = 0.25$ K h^{-1} (B, C, C2) with $N = (512^3, 1024^3, 2048^3)$ are denoted by line colors (green, black, red), respectively. Simulation F2 with $C_r = 1$ K h^{-1} and $N = 2048^3$ is presented in blue. Vertical profiles of average shear and buoyancy frequency squared (S^2, N^2), indicated by (solid, dashed) lines, respectively, are shown in the **right panel**.

Figures 2 and 3 also illustrate a strong dependence on bulk stratification in the SBL. The bulk stability measure h/L_{mo} increases from 1.56 to 5.77 as the cooling rate varies from $C_r = 0.25$ to 1 K h^{-1}. Increasing stratification leads to a decrease in the SBL turbulence level and as a result the height of the low-level jet (LLJ) descends from $z/h = 0.8$ to 0.58, i.e., from 105 m to 83 m. Then the wind veering in F2 is sharper and compressed in the lower SBL compared to C2. In F2, notice that the SBL is nearly equally split between the vertical layers below and above the LLJ. The mean wind, temperature, shear, and buoyancy profiles all change markedly above the LLJ compared to their counterparts in the lower SBL. Compensating for changes in the shear and buoyancy profiles leads to a relatively uniform $Ri \sim 0.2$ profile above the LLJ, which supports weak stratified turbulence. A further discussion of the impacts of increasing stratification on SBL statistics is given in [20].

The velocity variances from simulations (B, C, C2), which include the SFS contribution $2\langle e \rangle/3$, collapse reasonably well for the three mesh resolutions considered, as shown in Figure 4. The momentum and temperature fluxes $\langle u'w', v'w', w'\theta' \rangle$ that include both the resolved and SFS contributions are in close agreement as the mesh spacing varies from $\triangle = (0.78, 0.39, 0.20)$; see Figure 5. The profile of SFS energy $\langle e \rangle$, shown in Figure 6, shows a systematic decrease with resolution over the bulk of the SBL. For example, at $z/h = 0.5$ the scaling relationship $e \propto \triangle^{2/3}$ holds [36] (p. 589). The results in Figure 6 find a 40% decrease in e for a mesh-size reduction from 0.78 m to 0.2 m. Based on these results, we judge the LES results to be well converged.

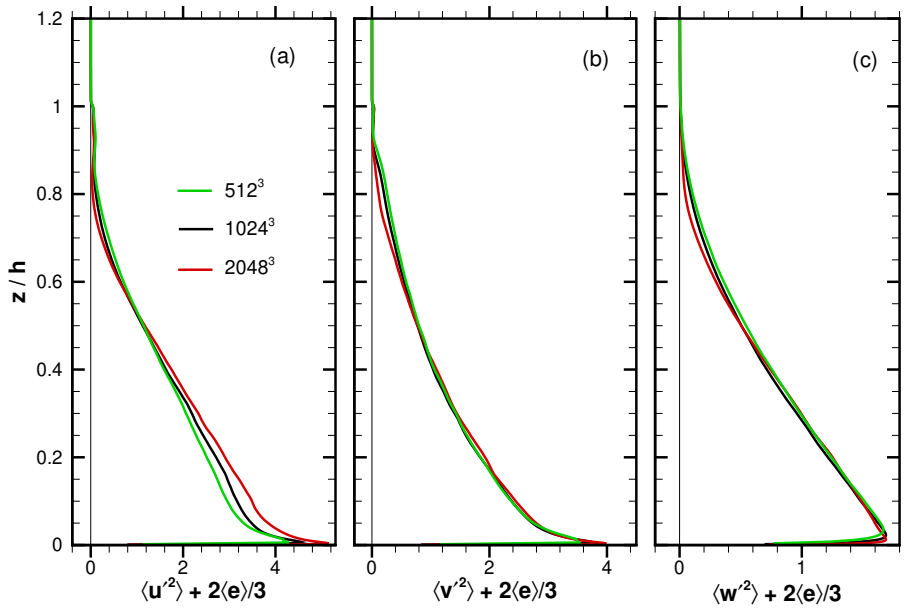

Figure 4. Vertical profiles of velocity variances $\langle u'^2, v'^2, w'^2 \rangle / u_*^2$ (panels (**a**)–(**c**), respectively). The variances include an estimate of the SFS contribution $2\langle e \rangle / 3$. Results are from simulations (B, C, C2) with $N = (512^3, 1024^3, 2048^3)$ denoted by line colors (green, black, red), respectively. The vertical coordinate is normalized by the SBL height h from each simulation.

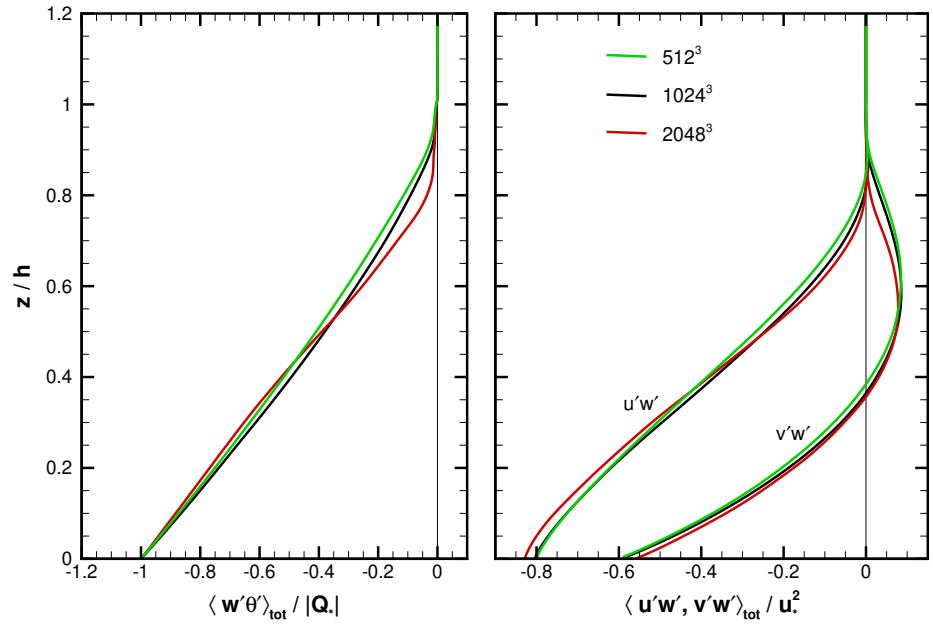

Figure 5. Vertical profiles of average temperature flux (**left panel**) and momentum fluxes (**right panel**). The fluxes are normalized by Q_* and u_*^2 as appropriate. The fluxes include the SFS contributions. Results are from simulations (B, C, C2) with $N = (512^3, 1024^3, 2048^3)$, denoted by line colors (green, black, red), respectively. The vertical coordinate is normalized by the SBL height h from each simulation.

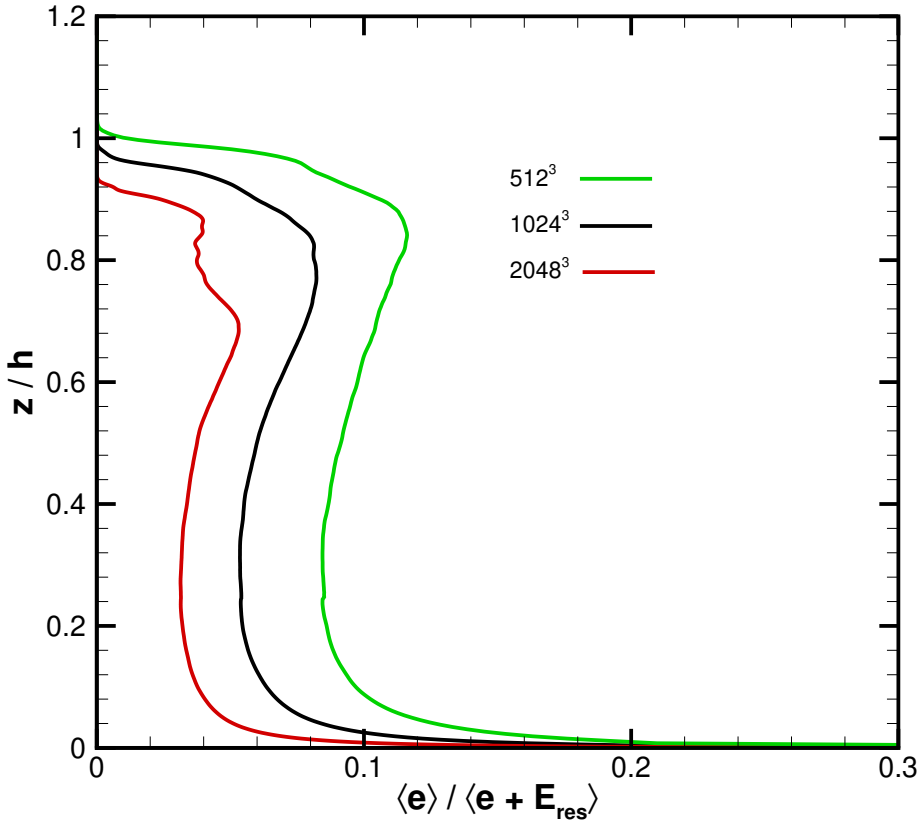

Figure 6. Vertical profile of SFS energy in the LES as a fraction of the total energy $\langle e \rangle / \langle e + E_{res} \rangle$ for different meshes $N = (512^3, 1024^3, 2048^3)$ denoted by (green, black, red) lines, respectively. The resolved kinetic energy $E_{res} = (u'^2 + v'^2 + w'^2)/2$.

5.2. Structures in Stable Boundary Layers

Flow visualization is extensively utilized to identify turbulent structures in the SBL; an example is provided in Figure 7. This image shows the instantaneous temperature isolines in an x–z plane from simulations C2 and F2 with weak and strong stratification, respectively. Inspection of the images shows an abundance of tightly compressed contour lines sprinkled throughout the SBL; the sharp gradients in θ are signatures of warm–cold temperature fronts passing through the domain. Notice that the temperature fronts are very sharp and tilted in the downstream direction, primarily a consequence of the sheared streamwise velocity $\langle u \rangle(z)$. Animations show the spatial and temporal evolution of the fronts (not shown). Frequently, the fronts are observed to extend over the full depth of the SBL and nearly the full horizontal extent of the domain, as shown in the upper panel of Figure 7. Turbulent mixing between fronts at different z levels leaves voids with nearly constant temperatures. Thus, at a fixed x–y location a vertical profile of θ displays a staircase pattern as different front families are crossed. As the stratification increases, the fronts tilt farther downstream and the separation between fronts shrinks considerably, as shown in the lower panel of Figure 7. A horizontal slice through the domain at $z/L_{mo} = 0.164$ m from simulation C2 provides a sense of the front coherence in the spanwise direction as well as the spatial randomness of the fronts. Figure 8 shows multiple fronts at various positions in the horizontal domain; the spanwise extent of a front is ∼50 m or less. At this instance in the simulation the warm upstream side of the front is modestly stronger than the cool downstream side of the front.

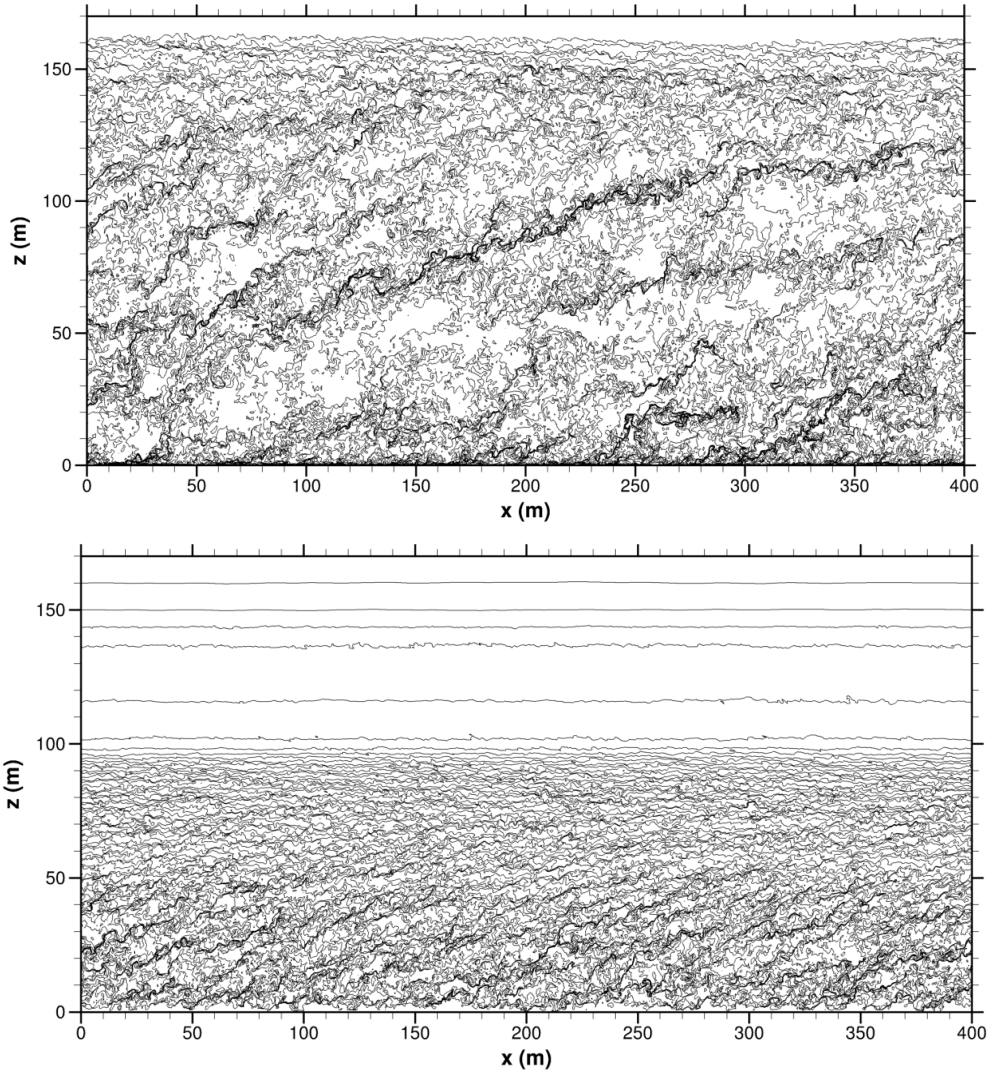

Figure 7. Temperature isolines in an x–z plane from simulations with weak surface cooling (**C2 upper panel**) and strong surface cooling (**F2 lower panel**) at $t \sim (8.556, 8.352)$ h, respectively. In the upper panel there are 51 contour levels between $(-2 < \theta - \theta_{ref} < 0)$ °C. In the lower panel there are 71 contour levels between $(-7.5 < \theta - \theta_{ref} < 0)$ °C. In addition, in the lower panel, contour levels $(0.2, 0.4, 0.5, 0.6)$ °C are shown for $z > 135$ m. The reference temperature $\theta_{ref} = 265$ K.

Linear stochastic estimation (LSE) pioneered by Adrian [56] is used to compute the conditional averages of the turbulent fields in the SBL. Our application of LSE [20] uses an event trigger based on a positive–negative temperature jump separated by a finite distance in a horizontal plane. This event choice is guided by the instantaneous flow visualization of θ' shown in Figure 8, which depicts numerous warm–cool temperature fronts. As an example, our LSE temperature event with $E = \pm 0.1$ K corresponds to a scalar flux about five times the surface value $|Q_*|$. The conditional fields $(\widehat{\mathbf{u}}, \widehat{p}, \widehat{\theta})$, velocity gradient tensor $\partial_j \widehat{u}_i$, and vorticity $\nabla \times \widehat{\mathbf{u}}$ are estimated for a range of vertical locations, spatial separation, and event amplitudes [20]. Our conditional sampling finds pairs of counter-rotating vortices in the SBL, as shown in Figure 9. The vortices are aligned with the mean wind direction and are tilted forward in the downstream direction. The upstream vortices act in concert to pump warm fluid forward while the downstream vortices pump cool fluid backwards, resulting in a near-stagnation point in the region between the vortices. The front boundary is very sharp but the vortices creating the fronts are well-resolved coherent structures. Sullivan et al. [20] show that the scale of the vortices lies near the peak in the spectrum for θ and w. The coherent structures in the interior of a sheared SBL are considerably

different than the pancake vortices in large-scale stably stratified turbulence away from a boundary [57].

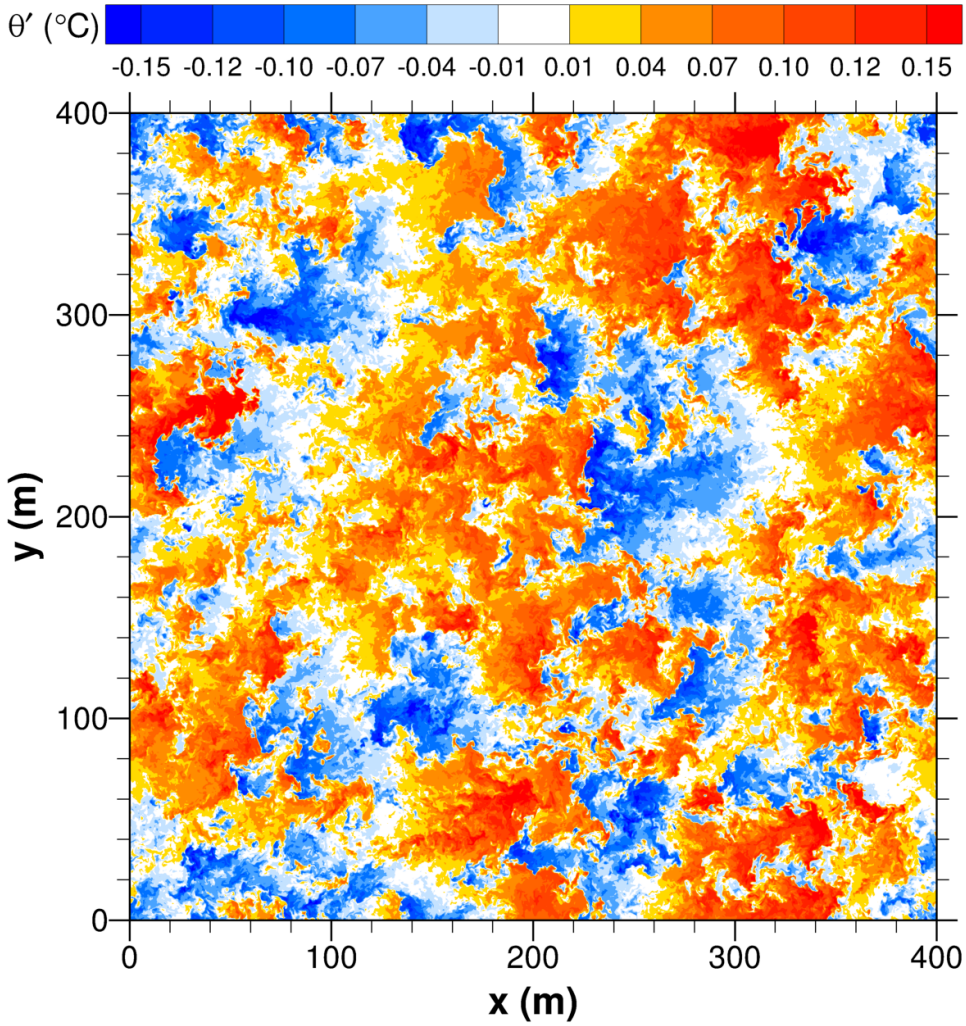

Figure 8. Fluctuating temperature field θ' at $z/L_{mo} = 0.164$ from simulation C2 at $t = 8.556$ h. Examples of sharp warm–cold temperature fronts are located at (x, y) = (20, 230), (200, 270), (230, 50), (230, 220), (330, 340) m. The color bar for $\theta' = \theta - \langle\theta\rangle$ is in units of °C.

5.3. SFS Motions in Observations and LES

The HATS dataset contains a mix of variations in wind speed, stratification, and perturbations in the array configuration, i.e., the vertical location z_d and horizontal separation δy_d of the anemometers shown in Figure 1. To account for these variations in computing the SFS motions Sullivan et al. [37] introduced a resolution ratio $\Lambda_w/\triangle_f$. The filter scale $\triangle_f \propto \delta y_d$ and is isotropic in x–y; only 2D filtering is employed in HATS. The vertical velocity is used to define Λ_w for the following reasons: w is the least-resolved field in LES, w statistics closely follow Monin–Obukhov similarity relationships in the surface layer, and w impacts the vertical fluxes, which are key ingredients in LES and also large-scale models. The length scale $\Lambda_w = 2\pi\langle U\rangle\tau_p$ where $\langle U\rangle$ is the mean wind speed and τ_p is the Eulerian integral time scale for vertical velocity. The autocorrelation function for w is fit to the form $R_w(t) = \exp(-t/\tau_p)$. This equates to finding a spectral peak in the vertical velocity spectrum assuming a high wavenumber spectrum k^{-2}; see Kaimal and Finnigan [58] (p. 63), Sullivan et al. [37], and Horst et al. [30]. This definition of Λ_w is robust and accounts for the distance z above the surface and stratification. In HATS the resolution ratio spans the range $0.1 < \Lambda_w/\triangle_f < 10$.

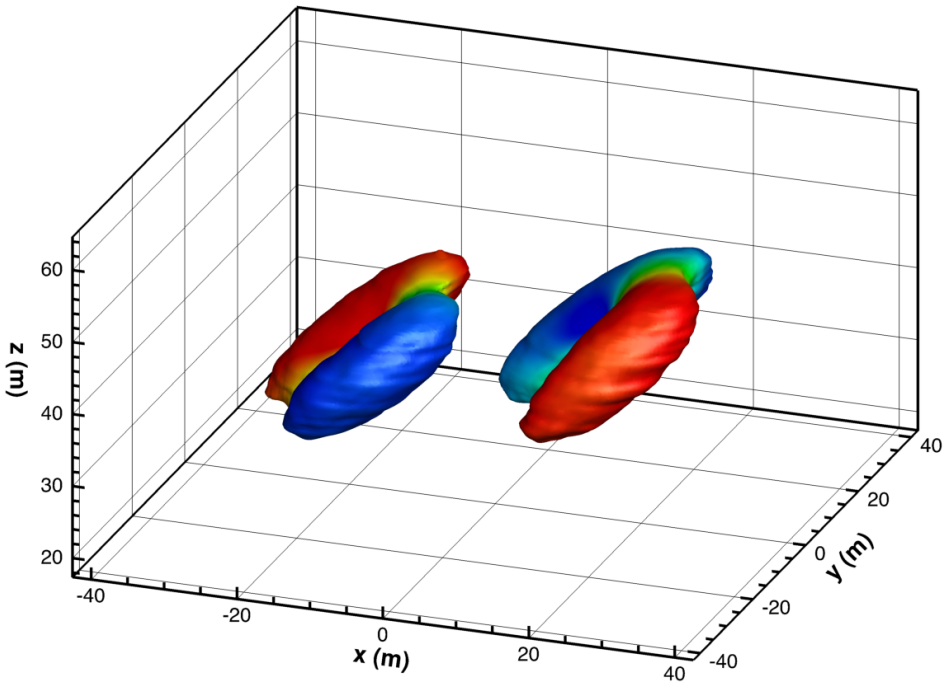

Figure 9. Oblique view of the typical 3D vortical structures in the SBL at a height $z/z_i = 0.2$ from simulation C with grid mesh of 1024^3 points [20] obtained using linear stochastic estimation-based conditional averaging. To indicate the sign of vortical rotation, the surface is colored by the vertical component of the vorticity vector $\zeta\ \hat{\mathbf{z}}$ with deep red (blue) colors corresponding to positive–upward (negative–downward) rotation, respectively. The mean horizontal winds are from left to right and at this height turn 30.6 degrees towards the $+y$ direction.

Physically, $\Lambda_w/\triangle_f$ is a measure of the scale separation between the large-scale energy-containing eddies and eddies near the filter scale, as sketched in Figure 10. For $\Lambda_w/\triangle_f \gg 1$ the separation is wide and the turbulence is well-resolved with the filter scale in the inertial range. Meanwhile, for $\Lambda_w/\triangle_f \leq 1$, the filter scale is near or left of the energy-containing eddies and the energy-containing turbulence is thus under-resolved. The ratio $\Lambda_w/\triangle_f$ is a measure of the simulation resolving power. When $\Lambda_w/\triangle_f \gg 1$ the simulation is LES and when $\Lambda_w/\triangle_f \ll 1$ the simulation is akin to unsteady Reynolds-Averaged Navier–Stokes (RANS). Wyngaard [40] calls the intermediate regime $\Lambda_w/\triangle_f \sim 1$ "Terra Incognita", which has similarity with the so-called gray zone [59,60]; it is unknown if the SFS closures used in LES or RANS are applicable in the gray zone. As $\Lambda_w/\triangle_f$ varies between the LES and RANS limits the length scale ℓ in an eddy-viscosity closure is predicted to vary linearly with the grid spacing $\ell \propto \min(\triangle, \ell_t)$ until $\triangle$ exceeds the scale of the energy-containing eddies ℓ_t, then ℓ becomes constant [61]. The crossover from LES to RANS is also recognized in the engineering community: Perot and Gadebusch [62] describe a two-equation self-adapting closure that spans the regime from DNS to LES to RANS for a mixing layer. Our estimate of a scale-aware length scale for dissipation in the SBL is discussed below.

To make a quantitative comparison between HATS and LES, we define the LES length scale Λ_w in terms of the spatial autocorrelation of vertical velocity $R_w(x, y)$, but aligned with the mean wind direction (see Figure 11). For LES, $\Lambda_w = 2\pi L_w$, where L_w is the integral scale obtained by integration of the autocorrelation $R_w(x', y' = 0)$ from $x' = 0$ to its first-zero crossing; Taylor's hypothesis is not used. The resolved fields $(\mathbf{u}, \theta)$, used to compute SFS motions, are also rotated into the mean-wind coordinate frame (x', y').

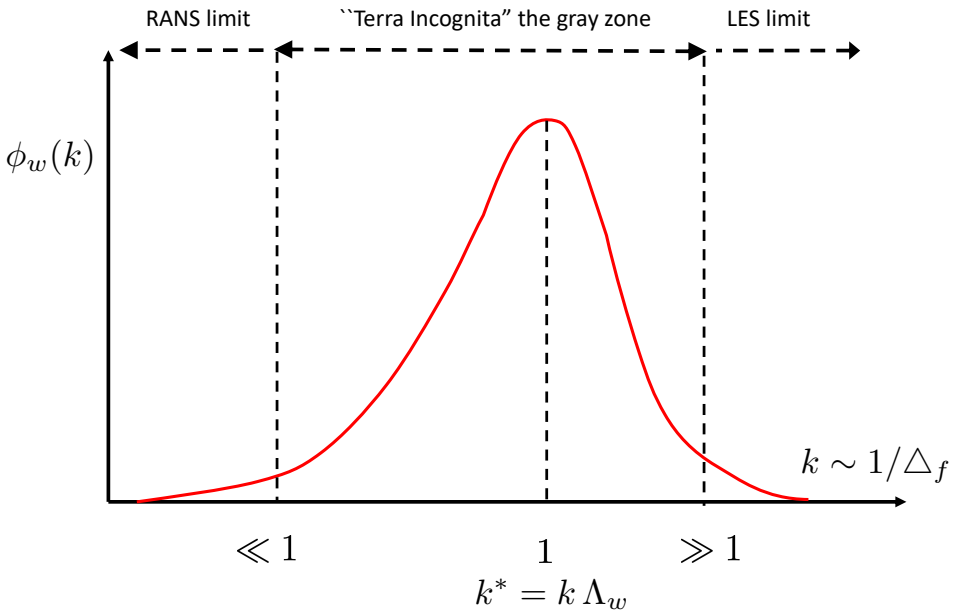

Figure 10. A sketch of the vertical velocity spectrum $\phi_w(k)$ in a horizontal plane as function of the horizontal wavenumber magnitude k. Its peak is at the non-dimensional wavenumber $k^* = k\,\Lambda_w = \Lambda_w/\triangle_f = 1$. The limits $k^* = \Lambda_w/\triangle_f \gg 1$ and $k^* = \Lambda_w/\triangle_f \ll 1$ are the LES and RANS regimes, respectively. In between these two limits is "Terra Incognita" or the gray zone. Figure is adapted from Wyngaard [40].

Analysis of the LES fields uses a filter scale $\triangle_f$ referenced to the scale $\triangle_c$ used in its subgrid model. For simulation C2 with the 2048^3 mesh and uniform spacing in all three directions the length scale in the subgrid model is $\triangle_c = (9/4)^{1/3}\triangle = 0.25$ m. Filter scales in the range $5 < \triangle_f/\triangle_c < 1000$ are used in the present analysis. The lower limit is chosen to help minimize contamination from the subgrid model while the upper limit is constrained by the horizontal dimensions of the LES box, 400 m in each direction. The turbulent fields at vertical levels $z/L_{mo} = (0.083, 0.164)$ inside and near the top of the surface layer are analyzed; at these two levels $\Lambda_w = (21.1, 26.7)$ m. Thus, the resolution ratio possible with the LES data spans $0.1 < \Lambda_w/\triangle_f < 20$, which nicely overlaps with the HATS data. The spatial filtering is a simple top-hat filter applied sequentially in the x–y directions, and the results from ten volumes are averaged to construct the SFS statistics. The SFS momentum and temperature fluxes, in both observations and LES, are constructed from:

$$\tau_{ij} = \widehat{u_i u_j} - \widehat{u}_i \widehat{u}_j \quad \text{and} \quad \tau_{i\theta} = \widehat{u_i \theta} - \widehat{u}_i \widehat{\theta}\,, \tag{4}$$

where the overhat notation $\widehat{(\,)}$ denotes two-dimensional x–y spatial filtering at $\triangle_f$.

The variation in the SFS velocity variances $\langle \tau_{11}, \tau_{22}, \tau_{33} \rangle$, momentum fluxes $\langle \tau_{12}, \tau_{13} \rangle$, and temperature fluxes $\langle \tau_{1\theta}, \tau_{3\theta} \rangle$ with varying resolution ratio $\Lambda_w/\triangle_f$ from HATS, OHATS, and LES are shown in Figures 12–14, respectively. Because of physical constraints, OHATS employed only a single array with horizontal spacing $\delta y_d = 0.58$ m. As a result, the variation in $\Lambda_w/\triangle_f$ from OHATS is a consequence of weak diurnal changes and possible wave effects over the ocean. The small value of $\triangle_f$ pushes all the OHATS results towards large $\Lambda_w/\triangle_f \sim 6$ to 10. HATS employed four different array configurations and, coupled with a vigorous diurnal cycle, results in a wide range of the resolution ratio. Inspection of the HATS data shows stratification is important, as the spectral peak in vertical velocity shifts from large to small scales as the stratification transitions from unstable to stable [58]. For example, the results from HATS array-1 at $z_d = 4.18$ m, blue bullets in Figure 12, span nearly a decade in $\Lambda_w/\triangle_f$ as $-0.3 < z_d/L_{mo} < 1.6$ (see Sullivan et al. [37]).

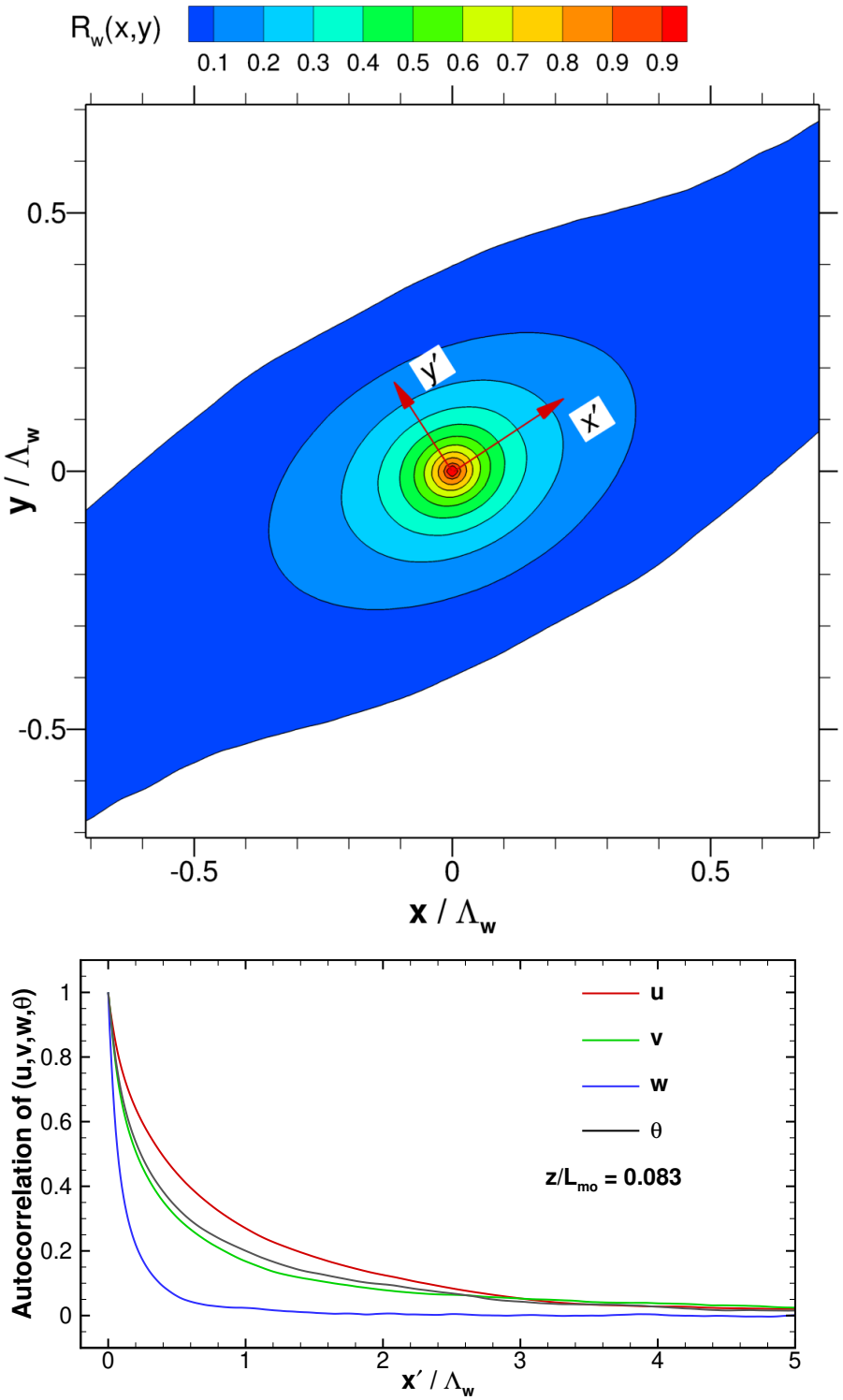

Figure 11. Two-dimensional autocorrelation for vertical velocity $R_{ww}(x, y)$ at $z/L_{mo} = 0.083$ from simulation C2 at $t = 8.556$ h (**upper panel**). The 1d correlation, extracted from the 2d correlation, for (u, v, w, θ) aligned with the mean wind direction x' at $y' = 0$ (**lower panel**). The peak wavelength for the w correlation is $\Lambda_w = 21.0$ m.

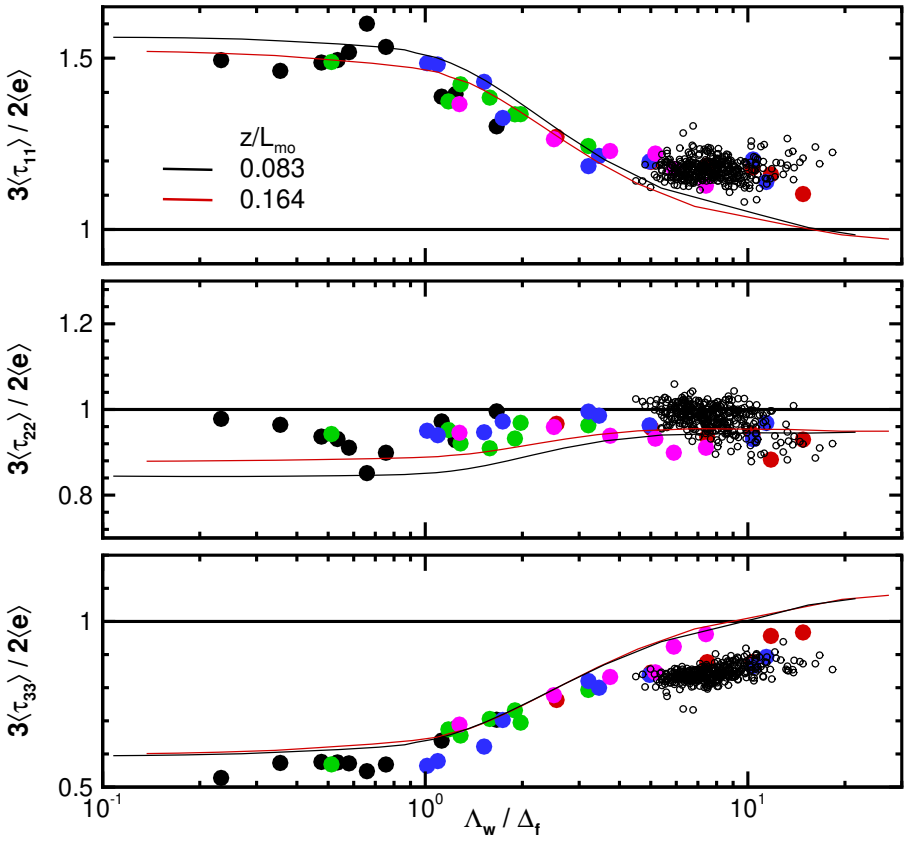

Figure 12. Variation of subfilter-scale velocity variances with resolution ratio $\Lambda_w/\triangle_f$. Measurements are collected in the atmospheric surface layer over land (colored bullets are from different sonic arrays in HATS) and over the ocean (open circles from OHATS) [37,47]. The (red, black) lines are filtered results from simulation C2 with mesh 2048^3. The (red, black) lines are in the surface layer $z/L_{mo} = (0.164, 0.083)$, respectively. The measurements and simulation results highlight the deviation from isotropy when the resolution ratio is $\Lambda_w/\triangle_f \sim \mathcal{O}(1)$.

Overall, the qualitative agreement between the simulation results and observations for variances and fluxes is good, and in some instances the comparison is quantitatively good. The normal variances τ_{ii} in Figure 12 are essentially a bulk metric of SFS isotropy. The observations and simulations both show that the variances $\langle\tau_{ii}\rangle$ tend to unity only for large $\Lambda_w/\triangle_f \geq 10$; isotropy at small scales is an implicit assumption in most Smagorinsky closures for LES, and thus fine computational grids are apparently needed to satisfy this metric. For $\Lambda_w/\triangle_f \leq 1$ the ratio $\langle\tau_{11}\rangle/\langle\tau_{33}\rangle > 2.3$ indicates high anisotropy in the peak energy-containing eddies in the streamwise and vertical components. The momentum fluxes $\langle\tau_{12}, \tau_{13}\rangle$ computed from LES fields are in good agreement with the observations. Notice the vertical momentum flux shows an expected steady approach towards $-u_*^2$ at small $\Lambda_w/\triangle_f$ at the level $z/L_{mo} = 0.083$. The results also suggest that the $z/L_{mo} = 0.164$ level is slightly outside the surface layer in the SBL. At small values of $\Lambda_w/\triangle_f \leq 0.4$, the LES results show a departure of the horizontal variance $\langle\tau_{22}\rangle$ from isotropy, qualitatively consistent with the measurements but perhaps to a somewhat greater degree. The LES also shows non-zero values of horizontal momentum flux $\langle\tau_{12}\rangle$, while the measurement scatter is too great to confidently assess this.

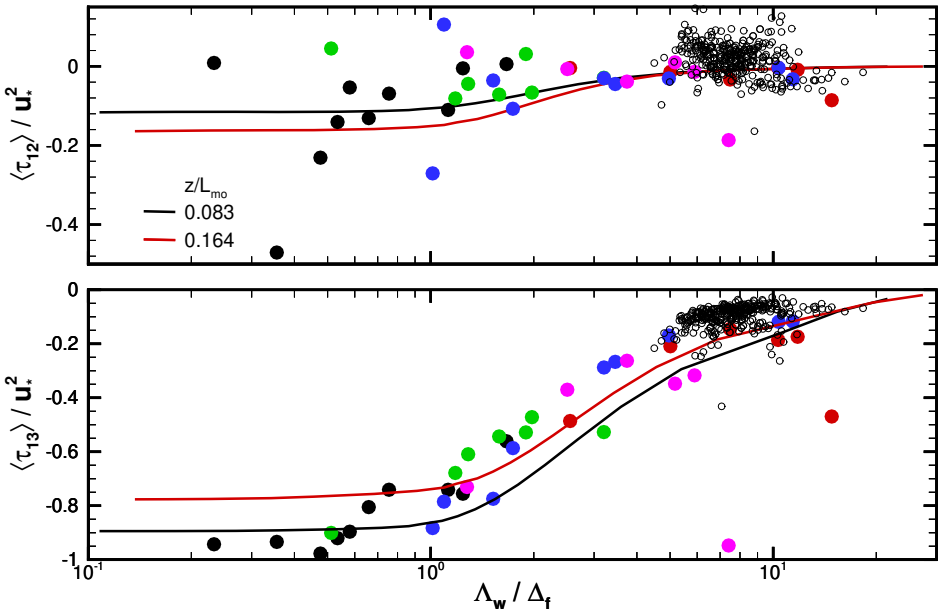

Figure 13. Variation of subfilter-scale momentum fluxes with varying resolution ratio $\Lambda_w/\triangle_f$. Horizontal momentum flux $\langle u'v'\rangle_{sfs}/u_*^2$ (**upper panel**) and vertical momentum flux $\langle u'w'\rangle_{sfs}/u_*^2$ (**lower panel**). Measurements are collected in the atmospheric surface layer over land (colored bullets) and ocean (open circles) [37,47]. The (red, black) lines show filtered results from simulation C2 with mesh 2048^3 and spacing $\triangle = 0.2$ m. The (red, black) lines are in the surface layer $z/L_{mo} = (0.164, 0.083)$, respectively. Note the different vertical scale in the upper and lower panels.

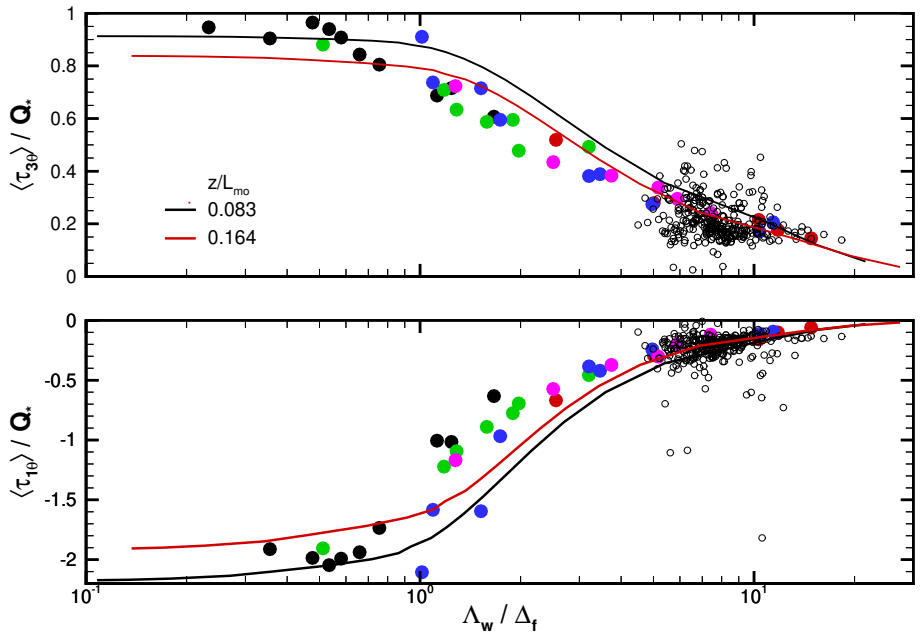

Figure 14. Variation of subfilter-scale temperature fluxes with varying resolution ratio $\Lambda_w/\triangle_f$. Horizontal flux $\langle u'\theta'\rangle_{sfs}/Q_*$ (**upper panel**) and vertical flux $\langle w'\theta'\rangle_{sfs}/Q_*$ (**lower panel**). Measurements are collected in the atmospheric surface layer over land (colored bullets) and over the ocean (open circles) [37,47]. The (red, black) lines show the filtered results from simulation C2 with mesh 2048^3. The (red, black) lines are in the surface layer $z/L_{mo} = (0.164, 0.083)$, respectively.

The horizontal and vertical scalar fluxes $\langle \tau_{1\theta}, \tau_{3\theta}\rangle$ are interesting. These SFS fluxes from LES are in good agreement with the observations. Notice as $\Lambda_w/\triangle_f \to 0$ the vertical scalar flux tends to the surface flux Q_* as expected while the horizontal scalar flux tends

to -2.5, which agrees very well with the HATS observations and also with the classic Kansas results, where Wyngaard et al. [63] find the ensemble average of the total scalar flux $-\langle u'\theta'\rangle/\langle w'\theta'\rangle \approx 2.5$ at large positive values of the stability parameter $z/L_{mo} \sim 0.6$. Based on the equations for scalar flux, Wyngaard [61] points out that $\langle \tau_{1\theta}\rangle$ is produced by tilting of the vertical scalar flux by vertical shear $\partial_z\langle u\rangle$, not by a horizontal gradient $\partial_x\langle\theta\rangle$, i.e., an eddy viscosity model is inadequate for horizontal scalar flux when $\Lambda_w/\triangle_f$ is small. Dynamically, the tilted vortices in Figure 9 are the agent producing horizontal scalar flux, as discussed in [20].

The average SFS variances and fluxes from LES agree well with the HATS and OHATS observations over a wide range of $\Lambda_w/\triangle_f$, and thus we expect the instantaneous spatially varying SFS motions from LES are also representative of atmospheric surface-layer flows. The visualizations in Figures 15–17 show the vertical momentum flux and vertical and horizontal temperature flux in the horizontal planes at level $z/L_{mo} = 0.164$ m for resolution ratios $\Lambda_f/\triangle_f = (0.15, 0.91, 2.09, 10.4)$, i.e., spanning either side of the gray zone. Inspection of the figures shows a smooth transition with varying $\Lambda_w/\triangle_f$. A parameterization needs to model all of the flux when $\Lambda_w/\triangle_f$ is small and stochastic fluctuations at large $\Lambda_w/\triangle_f$. In the intermediate gray zone the SFS motions contain a fraction of the total flux (see Figure 13), but stochastic fluctuations are also clearly present at the same time, e.g., see the visualization in Figure 15.

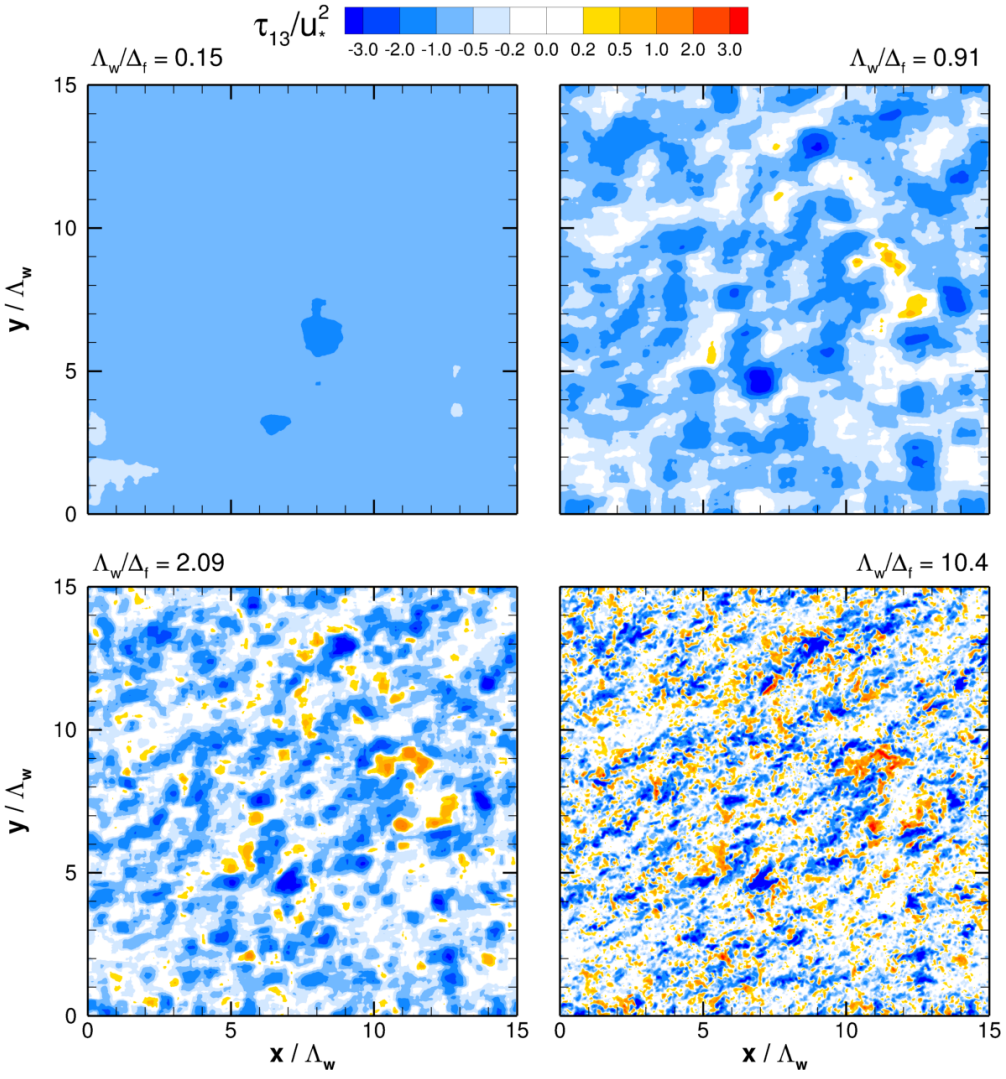

Figure 15. Subfilter-scale momentum flux τ_{13} at $z/L_{mo} = 0.164$ m with varying resolution ratio $\Lambda_w/\triangle_f = (0.52, 0.91, 2.09, 10.4)$ from simulation C2. The normalization is by u_*^2.

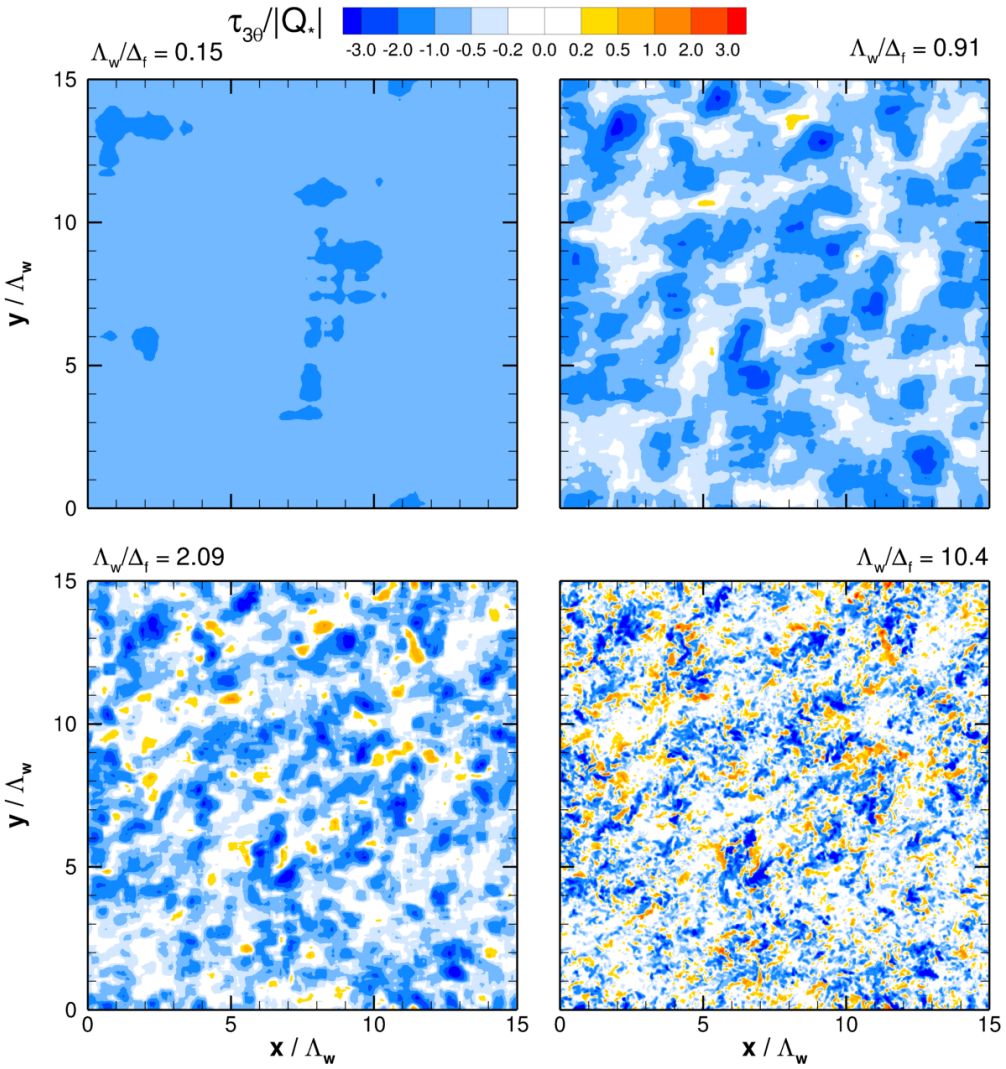

Figure 16. Subfilter-scale vertical temperature flux $\tau_{3\theta}/|Q_*|$ at $z/L_{mo} = 0.164$ with varying resolution ratio $\Lambda_w/\triangle_f = (0.15, 0.91, 2.09, 10.4)$ from simulation C2. To preserve the sign of the flux the normalization is by $|Q_*|$.

In the gray zone, to ensure the proper energy transfer between the resolved and subgrid fields, a SFS flux parameterization needs to account for a fraction of the net flux plus fluctuations correlated with the fluctuating strain rate. To illustrate the idea, consider the energy equation for the resolved motions, which contains the transfer term $\tau_{ij}S_{ij}$, where S_{ij} is the resolved rate of strain tensor; recall this term also appears in the SFS energy equation with opposite sign [64]. Decomposing the SFS flux and resolved rate of strain tensors into a mean and fluctuation yields the expression

$$\langle \tau_{ij} S_{ij} \rangle \;=\; \langle \tau_{ij} \rangle \langle S_{ij} \rangle \;+\; \langle \tau'_{ij} S'_{ij} \rangle \;; \tag{5}$$

notice that $\tau'_{ij}S'_{ij}$ allows both forward and backward (backscatter) motion of energy, which was observed in HATS [37]. Inspection of (5) shows the difficulty: energy transfer at small and large $\Lambda_w/\triangle_f$ is $\langle \tau_{ij} \rangle \langle S_{ij} \rangle$ or the turbulent correlation $\langle \tau'_{ij} S'_{ij} \rangle$, respectively. However, Figure 18 shows that in the intermediate gray zone both terms on the right-hand side of (5) contribute to the energy transfer. Thus, a SFS flux parameterization needs to account for a fraction of the net flux but also important stochastic fluctuations because of the energy transfer between the resolved and subgrid fields. The SFS momentum fluctuations are not random noise but are clearly correlated with fluctuations in the strain rate. The transfer of scalar variance faces a similar dilemma in the gray zone.

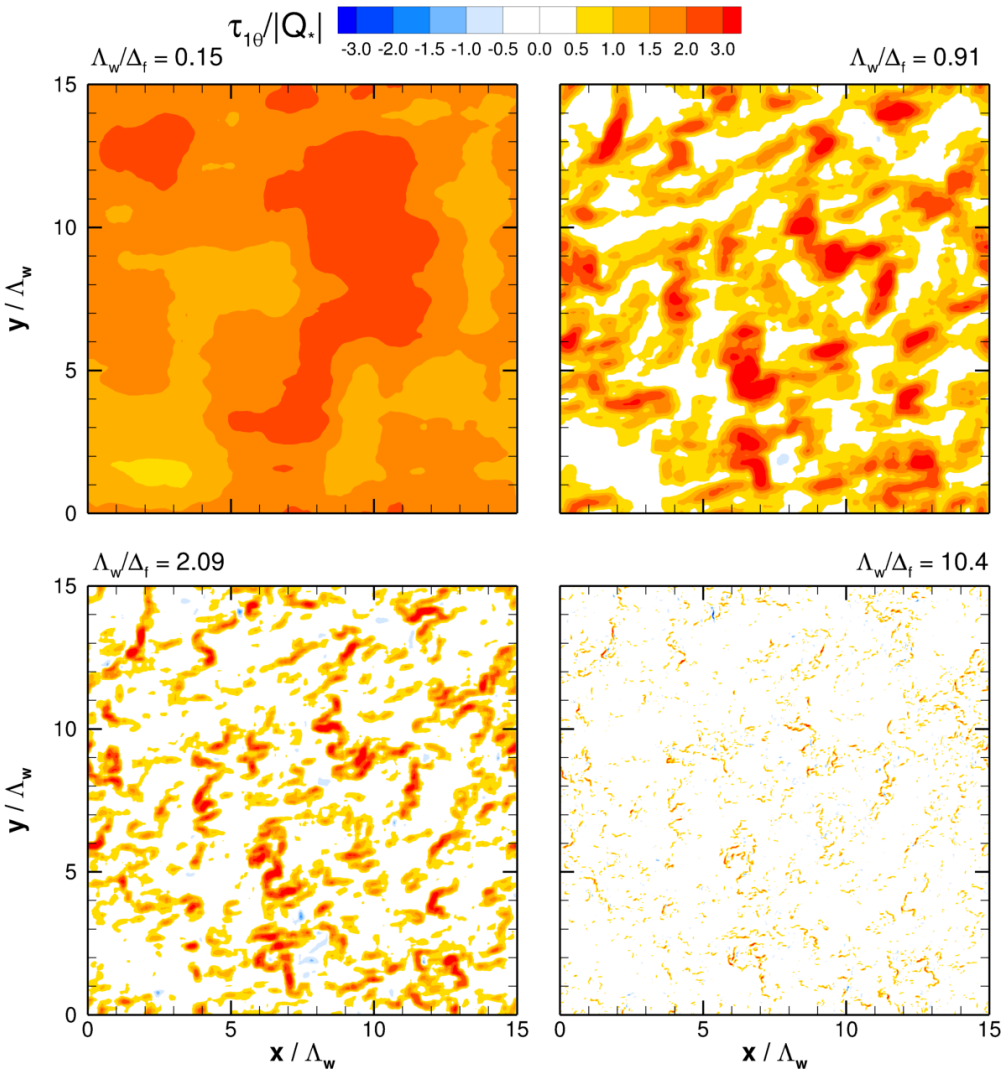

Figure 17. Subfilter-scale horizontal temperature flux $\tau_{1\theta}/|Q_*|$ at $z/L_{mo} = 0.164$ with varying resolution ratio $\Lambda_w/\triangle_f = (0.52, 0.91, 2.09, 10.4)$ from simulation C2. To preserve the sign of the flux the normalization is by $|Q_*|$.

Parameterizations in the gray zone are further confronted by the possible "double counting" of the momentum and temperature fluxes. This can result when a SFS paramterization is used outside its design range in the space $\Lambda_w/\triangle_f$. For example, this can occur in the gray zone $\Lambda_w/\triangle_f \sim 1$ when a single-column model, designed for RANS vertical flux, is used at the same time the model grid resolution is sufficient to support the resolved turbulence. Under these conditions the estimate of flux can be double counted [60]. Flux double counting spoils the energy and scalar transfer between the resolved and SFS fields.

A cursory inspection of the patterns in τ_{13} (Figure 15) and $\tau_{3\theta}$ (Figure 16) suggests a possible amplitude correlation, i.e., $\tau_{3\theta}$ is approximately related to τ_{13} by a constant [65]. The assumption that the scalar diffusivity and momentum eddy viscosity are related is routinely adopted by LES models. The visualization of the streamwise scalar flux shows a near-zero mean and small fluctuations at large $\Lambda_w/\triangle_f$; $\tau_{1\theta}$ is routinely neglected in SFS modeling [66]. At small $\Lambda_w/\triangle_f$ the horizontal scalar flux is clearly non-zero, but its impact disappears under the usual assumption of a periodic horizontally homogeneous flow $\partial_x\langle u'\theta'\rangle = 0$.

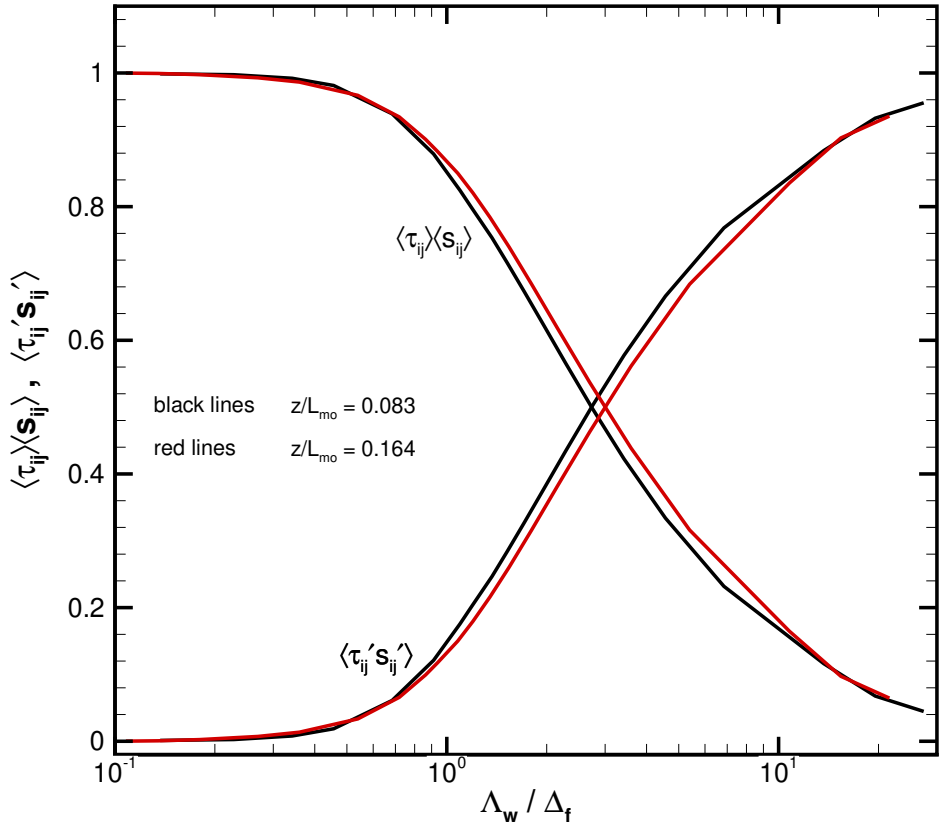

Figure 18. Variation of the production terms in Equation (5) for varying filter width $\triangle_f$ at two heights near the surface $z/L_{mo} = (0.083, 0.164)$ denoted by (black, red) lines, respectively, from simulation C2. The individual production terms are normalized by the total production $\langle \tau_{ij} S_{ij} \rangle$ at each filter width. Total production $\langle \tau_{ij} S_{ij} \rangle$ is nearly constant with varying $\triangle_f$, but slopes downward at small filter widths because of the actual subgrid model used in the LES.

The fine-mesh LES results can also be used to craft parameterizations that span the gray zone. For example, consider a $q^2 - \ell$ second-order closure that uses a prognostic equation for the unresolved SFS turbulence kinetic energy $q^2 = (u'^2 + v'^2 + w'^2)/2$ with ℓ a prescribed length scale. This closure uses a TKE equation with a model for viscous dissipation ϵ [65], typically of the form

$$\epsilon = \frac{q^3}{L_\epsilon} \,. \tag{6}$$

The dissipation model requires specification of the length scale L_ϵ. Figure 19 shows the variation of L_ϵ with inverse resolution ratio $\triangle_f / \Lambda_w$ computed from the LES results; this result is obtained by assuming a constant dissipation across $\triangle_f$. For small filter widths in the LES regime, q^2 is a small fraction of the total energy and $L_\epsilon \propto \triangle_f$. At large filter widths approaching the RANS regime, q^2 is the total kinetic energy and the length scale saturates, i.e., $L_\epsilon / \Lambda_w \sim 1.4$ in the surface layer. A smooth variation of L_ϵ is found at intermediate filter widths between the RANS and LES limits. In the middle of the gray zone $L_\epsilon \sim \Lambda_w$ at $\triangle_f = \Lambda_w$. Thus, in general one needs an adaptive parameterization $L_\epsilon = L_\epsilon(z, \triangle_f / \Lambda_w)$ as the filter width varies across the RANS to LES regimes.

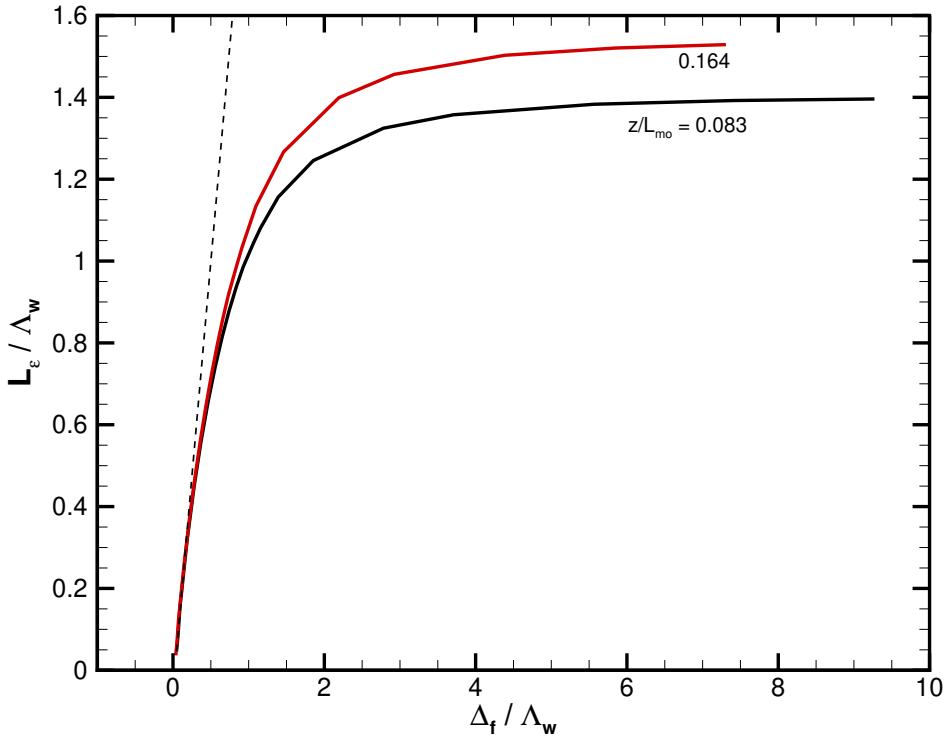

Figure 19. Variation of the dissipation length scale L_ϵ for varying filter width $\triangle_f$ at two heights near the surface $z/L_{mo} = (0.083, 0.164)$ denoted by (black, red) lines, respectively, from simulation C2. The black dashed line is a linear fit to L_ϵ for small filter widths similar to the predictions by Wyngaard [61].

6. Summary and Discussion

Recent high-resolution large-eddy simulations (LES) of a stable atmospheric boundary layer (SBL) with mesh sizes $N = (512^3, 1024^3, 2048^3)$, or mesh spacings $\triangle = (0.78, 0.39, 0.2)$ m, are described and analyzed. The SBL posing is the GABLS1 intercomparison case for LES driven by a constant surface cooling rate $C_r = 0.25$ K h^{-1} described by Beare et al. [24] and Holtslag [23]. An SBL with a nearly four-times-stronger stratification on a mesh with $N = 2048^3$ is also analyzed. These recent high-resolution datasets with 2048^3 mesh points are being added to the Johns Hopkins University Turbulence Database (JHTDB) for further analysis by the research community.

The LES solutions on meshes $N = (512^3, 1024^3, 2048^3)$ are judged converged based on the good collapse of vertical profiles of mean winds, temperature, and low-order turbulence moments, i.e., fluxes and variances. The largest discrepancy is in the stably stratified region above the low-level jet (LLJ) where the turbulence is small-scale and weak. The boundary-layer height between the simulations varies by less than 10%, which induces small changes in the friction velocity and surface temperature flux. These comparisons with different N indicate that further convergence of low-order moments is likely with even larger values. With increasing stratification, $C_r = 1$ K h^{-1}, the LLJ descends and the SBL is nearly equally split into two vertical layers. Above the LLJ the Richardson number is uniform $Ri \sim 0.2$, which supports only weak turbulence.

The flow visualization shows the SBL is filled with ubiquitous temperature fronts tilted in the streamwise direction. The spatial distance separating the warm–cold fronts is thin, i.e., the fronts are very sharp. Mesh refinement decreases the spatial separation between the fronts, and increasing stratification causes the fronts to tilt farther forward in a shallower SBL. At a fixed horizontal location x–y a temperature profile exhibits a staircase pattern in the vertical direction where sharp jumps are separated by a nearly uniform (constant) temperature. The flow visualization highlights the SBL dynamics across scales. Pairs of counter-rotating, well-resolved "horseshoe" vortices tilted in the downstream–upward direction are the agents inducing the sharp temperature fronts; the vortices induce

both vertical and horizontal temperature and momentum fluxes. The scale of the vortices coincides with the scale of the peak in the θ and w spectra, as shown by Sullivan et al. [20].

The subfilter-scale (SFS) motions deduced from the LES solutions are compared with observations from the horizontal array turbulence study (HATS) and the ocean horizontal turbulence study (OHATS); these multi-point measurements were collected from cross-wind arrays of sonic anemometers in the atmospheric surface layer over a range of wind speeds, stratification, and sensor spacings. The SFS momentum and temperature fluxes, $\tau_{ij} = \widehat{u_i u_j} - \widehat{u}_i \widehat{u}_j$ and $\tau_{i\theta} = \widehat{u_i \theta} - \widehat{u}_i \widehat{\theta}$, are constructed from the observations and LES using similar 2D low-pass filters with varying filter width $\triangle_f$. Their comparisons are carried out using a dimensionless resolution ratio $\Lambda_w/\triangle_f$, where Λ_w is the characteristic length scale of the energy-containing eddies for vertical velocity w. Over the range $0.1 < \Lambda_w/\triangle_f < 10$, the SFS fluxes and variances from the fine-mesh LES and observations are in good agreement. At first blush this seems surprising, but notice that when $\triangle_f \gg \triangle$ very-well-resolved turbulent motions are used to compute the SFS variances and fluxes.

The limits $\Lambda_w/\triangle_f > 10$ and $\Lambda_w/\triangle_f < 0.1$ correspond to the LES and unsteady Reynolds-averaged Navier–Stokes (RANS) regimes, respectively. The intermediate regime is encountered near walls and in simulations with coarse LES grids or fine mesoscale grids. The regime with $\Lambda_w/\triangle_f \sim 1$ is termed "Terra Incognita" or the gray scale by Wyngaard [40]. The SFS fluxes from HATS and LES both vary smoothly across the gray scale. The SFS parameterization in the gray scale with partially resolved flux needs to account for both a "RANS" flux in addition to fluctuations. Fluctuations in the SFS momentum fluxes are not random noise but are well correlated with the strain rate. A scale-aware parameterization needs to set the proper energy or scalar transfer between the resolved and subgrid fields.

The good agreement between the LES results and observations is encouraging and allows fine-mesh LES fields to be used for guidance in formulating SFS models and for a priori tests for the SBL and other high-Reynolds-number flows. These would be more relevant than similar tests with DNS that are limited to geophysically unrealistically low values of the Reynolds number. Given the large number of SFS parameterization models that have been proposed and the several canonical geophysical flow regimes, it would be a substantial enterprise to make systematic tests, but well worthwhile. Moreover, in the spirit of our age, one could ask whether artificial intelligence algorithms should supervise the tests or even search beyond the present SFS proposals.

7. Whither Turbulence?

This section title is shamelessly borrowed from Lumley [67], which is a collection of essays about the state and direction of turbulence research at that time. (See also the biographical discussion of Lumley's life and views in Leibovich and Warhaft [68]).

Turbulent flows are ubiquitous in natural fluids, and their science is centuries old. It is an unusual science in several ways. Its governing partial differential equation, Navier–Stokes, is known and seems to be valid after many experimental tests. Yet its mathematical nature is still incompletely characterized (n.b., the unclaimed Clay Mathematics Institute Millennium Prize for proof of existence and smoothness of its solutions). It is highly accessible to measurements in laboratories and Earth's atmosphere and ocean. Yet these measurements always seem to be insufficiently complete. It has been and continues to be a premier computational problem with various discrete approximations to the known continuum equations. Yet solution convergence remains elusive in pursuit of the very large Reynolds numbers in natural flows, and turbulence seems to have an endless variety of outcomes in different physical regimes. We remember Horace Lamb's quip about whether we would even understand the nature of turbulence if it were explained to us in heaven [69].

Thus, we just keep plugging away. Turbulence is far too important to abandon, and measurements and simulations can always answer whatever a well-conceived next question is. We can continue to make models of how turbulence behaves in the subgrid-scale regime

at high Reynolds number; they are at least useful, if not provably correct, and they are falsifiable with a next set of measurements and simulations. The solutions in this paper could play such a role for many extant models. The goal is to identify and solve problems that enable us to infer generic behaviors, recognizing that many different paradigms are needed for geophysical turbulence.

The present paper is a happy confluence of multi-point atmospheric measurements, apparently adequate subgrid parameterizations, and large computational grids that takes yet another step up the tall ladder toward heaven, where maybe we will meet Jack again.

Author Contributions: All authors contributed to the work. J.C.M. wrote critical sections of the manuscript, suggested analyses, and edited the manuscript. C.M. participated in HATS, edited the manuscript, and suggested analyses. E.G.P. ran simulations, edited the manuscript, and suggested analyses. P.P.S. participated in HATS and OHATS, ran simulations, analyzed the observational and simulation data, and wrote large sections of the manuscript. All authors have read and agreed to the published version of the manuscript.

Funding: CM, EGP, and PPS were supported by NSF award number 2103874 with the JHU to NCAR, subaward 2005117865. PPS and JCM were supported by the Office of Naval Research through the Physical Oceanography Program, award numbers N00014-17-1-2334 and N00014-18-1-2599, and by the National Oceanic and Atmospheric Administration, award number NA19OAR4310378. PPS and EGP acknowledge support from the National Science Foundation and the Geophysical Turbulence Program at the National Center for Atmospheric Research (NCAR). We also acknowledge high-performance computing support from Cheyenne (https://doi.org/10.5065/D6RX99HX, accessed on 7 June 2023) provided by NCAR's Computational and Information Systems Laboratory, sponsored by the National Science Foundation.

Institutional Review Board Statement: Not applicable.

Informed Consent Statement: Not applicable.

Data Availability Statement: The numerical simulation data used in this manuscript will be accessible via the Johns Hopkins Turbulence Database: https://turbulence.pha.jhu.edu (accessed on 7 June 2023). The HATS and OHATS data can be accessed at: https://doi.org/10.5065/D6X34VWV (accessed on 7 June 2023) and https://doi.org/10.5065/D6959G0N (accessed on 7 June 2023), respectively.

Acknowledgments: The authors thank James Edson (Woods Hole Oceanographic Institute), John Wyngaard (The Pennsylvania State University), and Thomas Horst (NCAR) for their participation in the OHATS field campaign. The five reviewers provided useful comments that improved the manuscript.

Conflicts of Interest: The authors declare no conflict of interest. The funders had no role in the design of the study; in the collection, analyses, or interpretation of data; in the writing of the manuscript; or in the decision to publish the results.

References

1. Patterson, G.; Orszag, S. Spectral calculations of isotropic turbulence: Efficient removal of aliasing interactions. *Phys. Fluids* **1971**, *14*, 2538. [CrossRef]
2. Herring, J.R.; McWilliams, J.C. Lecture Notes on Turbulence. In *Lecture Notes from the NCAR-GTP Summer School*; Herring, J.R., McWilliams, J.C., Eds.; World Scientific: Singapore, 1989; p. 371. [CrossRef]
3. Fernando, H.J.S. Turbulent mixing in stratified fluids. *Annu. Rev. Fluid Mech.* **1991**, *23*, 455–493. [CrossRef]
4. Fernando, H.J.S.; Weil, J.C. Whither the stable boundary layer? A shift in the research agenda. *Bull. Am. Meteorol. Soc.* **2010**, *91*, 1475–1481. [CrossRef]
5. Mahrt, L. Stably stratified atmospheric boundary layers. *Annu. Rev. Fluid Mech.* **2014**, *46*, 23–45. [CrossRef]
6. Caulfield, C.P. Layering, instabilities, and mixing in turbulent stratified flows. *Annu. Rev. Fluid Mech.* **2021**, *53*, 113–145. [CrossRef]
7. Large, W.G.; McWilliams, J.C.; Doney, S.C. Oceanic vertical mixing: A review and a model with a nonlocal boundary layer parameterization. *Rev. Geophys.* **1994**, *32*, 363–403. [CrossRef]
8. McWilliams, J.C. Phenomenological hunts in two-dimensional and stably stratified turbulence. In *Atmospheric Turbulence and Mesoscale Meteorology*; Federovich, E., Rotunno, R., Stevens, B., Eds.; Cambridge University Press: Cambridge, UK, 2004; pp. 35–49. [CrossRef]

9. Cuxart, J.; Holtslag, A.A.M.; Beare, R.J.; Bazile, E.; Beljaars, A.; Cheng, A.; Conangla, L.; Ek, M.; Freedman, F.; Hamdl, R.; et al. Single-column model intercomparison for a stably stratified atmospheric boundary layer. *Bound.-Layer Meteorol.* **2006**, *118*, 273–303. [CrossRef]
10. Svensson, G.; Holtslag, A.A.M. Analysis of model results for the turning of the wind and related momentum fluxes in the stable boundary layer. *Bound.-Layer Meteorol.* **2009**, *132*, 261–277. [CrossRef]
11. Holtslag, A.A.M.; Svensson, G.; Baas, P.; Basu, S.; Beare, B.; Beljaars, A.C.M.; Bosveld, F.C.; Cuxart, J.; Lindvall, J.; Steeneveld, G.J.; et al. Stable atmospheric boundary layers and diurnal cycles: Challenges for weather and climate models. *Bull. Am. Meteorol. Soc.* **2013**, *94*, 1691–1706. [CrossRef]
12. Heisel, M.; Sullivan, P.P.; Katul, G.G.; Chamecki, M. Turbulence organization and mean profile shapes in the stably stratified boundary layer: Zones of uniform momentum and air temperature. *Bound.-Layer Meteorol.* **2023**, *186*, 533–565. [CrossRef]
13. Wyngaard, J.C.; Seaman, N.; Kimmel, S.J.; Otte, M.; Di, X.; Gilbert, K.E. Concepts, observations, and simulation of refractive index turbulence in the lower atmosphere. *Radio Sci.* **2001**, *36*, 643–669. [CrossRef]
14. Kelley, N.; Shirazi, M.; Buhl, M.; Jager, D.; Wilde, S.; Adams, J.; Bianchi, J.; Sullivan, P.; Patton, E. *Lamar Low-Level Jet Project Interim Report*; Technical Report NREL/TP-500-34593; National Renewable Energy Laboratory: Golden, CO, USA, 2003. [CrossRef]
15. Weil, J.C. Stable boundary layer modeling for air quality applications. In *Air Pollution Modeling and Its Application XXI*; Castelli, S.T., Steyn, D., Eds.; NATO Science for Peace and Security Series C: Environmental Security; Springer: Dordrecht, The Netherlands, 2012; pp. 57–61. [CrossRef]
16. Nieuwstadt, F.T.M. Direct numerical simulation of stable channel flow at large stability. *Bound.-Layer Meteorol.* **2005**, *116*, 277–299. [CrossRef]
17. van de Wiel, B.J.H.; Moene, A.F.; Hartogensis, O.K.; de Bruin, H.A.R.; Holtslag, A.A.M. Intermittent turbulence in the stable boundary layer over land. Part III. A classification for observations during CASES-99. *J. Atmos. Sci.* **2003**, *60*, 2509–2522. [CrossRef]
18. van Haren, H.; Gostiaux, L. A deep-ocean Kelvin-Helmholtz billow train. *Geophys. Res. Lett.* **2010**, *37*, L03605. [CrossRef]
19. Moeng, C.H.; Sullivan, P.P. Large-eddy simulation. In *Encyclopedia of Atmospheric Sciences*, 2nd ed.; North, G.R., Zhang, F., Pyle, J., Eds.; Academic Press: Cambridge, MA, USA, 2015; Volume 4, pp. 232–240. [CrossRef]
20. Sullivan, P.P.; Weil, J.C.; Patton, E.G.; Jonker, H.J.J.; Mironov, D.V. Turbulent winds and temperature fronts in large-eddy simulations of the stable atmospheric boundary layer. *J. Atmos. Sci.* **2016**, *73*, 1815–1840. [CrossRef]
21. Johnson, P.L. A physics-inspired alternative to spatial filtering for large-eddy simulations of turbulent flows. *J. Fluid Mech.* **2022**, *934*, A30. [CrossRef]
22. Sullivan, P.P.; McWilliams, J.C.; Moeng, C.H. A subgrid-scale model for large-eddy simulation of planetary boundary-layer flows. *Bound.-Layer Meteorol.* **1994**, *71*, 247–276. [CrossRef]
23. Holtslag, A.A.M. GEWEX atmospheric boundary-layer study GABLS on stable boundary layers. *Bound.-Layer Meteorol.* **2006**, *118*, 243–246. [CrossRef]
24. Beare, R.J.; Macvean, M.K.; Holtslag, A.A.M.; Cuxart, J.; Esau, I.; Golaz, J.C.; Jimenez, M.A.; Khairoutdinov, M.; Kosovic, B.; Lewellen, D.; et al. An intercomparison of large-eddy simulations of the stable boundary layer. *Bound.-Layer Meteorol.* **2006**, *118*, 242–272. [CrossRef]
25. Huang, J.; Bou-Zeid, E. Turbulence and vertical fluxes in the stable atmospheric boundary layer. Part I: A large-eddy simulation study. *J. Atmos. Sci.* **2013**, *70*, 1513–1527. [CrossRef]
26. Li, Y.; Perlman, E.; Wan, M.; Yang, Y.; Meneveau, C.; Burns, R.; Chen, S.; Szalay, A.; Eyink, G. A public turbulence database cluster and applications to study Lagrangian evolution of velocity increments in turbulence. *J. Turbul.* **2008**, *9*, N31. [CrossRef]
27. Graham, J.; Kanov, K.; Yang, X.; Lee, M.; Malaya, N.; Lalescu, C.; Burns, R.; Eyink, G.; Szalay, A.; Moser, R.; et al. A web services accessible database of turbulent channel flow and its use for testing a new integral wall model for LES. *J. Turbul.* **2016**, *17*, 181–215. [CrossRef]
28. Piomelli, U.; Moin, P.; Ferziger, J.H. Model consistency in large eddy simulation of turbulent channel flows. *Phys. Fluids* **1988**, *31*, 1884–1891. [CrossRef]
29. Liu, S.; Meneveau, C.; Katz, J. On the properties of similarity subgrid-scale models as deduced from measurements in a turbulent jet. *J. Fluid Mech.* **1994**, *275*, 83–119. [CrossRef]
30. Horst, T.W.; Kleissl, J.; Lenschow, D.H.; Meneveau, C.; Moeng, C.H.; Parlange, M.B.; Sullivan, P.P.; Weil, J.C. Field observations to obtain spatially-filtered turbulence fields from transverse arrays of sonic anemometers in the atmospheric surface layer. *J. Atmos. Sci.* **2004**, *61*, 1566–1581. [CrossRef]
31. Meneveau, C.; Lund, T.S. The dynamic Smagorinsky model and scale-dependent coefficients in the viscous range of turbulence. *Phys. Fluids* **1997**, *9*, 3932–3934. [CrossRef]
32. Tong, C.; Wyngaard, J.C.; Khanna, S.; Brasseur, J.G. Resolvable- and subgrid-scale measurement in the atmospheric surface layer: Technique and issues. *J. Atmos. Sci.* **1998**, *55*, 3114–3126. [CrossRef]
33. Tong, C.; Wyngaard, J.C.; Brasseur, J.G. Experimental study of the subgrid-scale stresses in the atmospheric surface layer. *J. Atmos. Sci.* **1999**, *56*, 2277–2292. [CrossRef]
34. Tao, B.; Katz, J.; Meneveau, C. Geometry and scale relationships in high Reynolds number turbulence determined from three-dimensional holographic velocimetry. *Phys. Fluids* **2000**, *12*, 941–944. [CrossRef]

35. Meneveau, C.; Katz, J. Scale-invariance and turbulence models for large-eddy simulations. *Annu. Rev. Fluid Mech.* **2000**, *32*, 1–32. [CrossRef]
36. Pope, S.B. *Turbulent Flows*; Cambridge University Press: Cambridge, UK, 2000; p. 771. [CrossRef]
37. Sullivan, P.P.; Horst, T.W.; Lenschow, D.H.; Moeng, C.H.; Weil, J.C. Structure of subfilter-scale fluxes in the atmospheric surface layer with application to large-eddy simulation modeling. *J. Fluid Mech.* **2003**, *482*, 101–139. [CrossRef]
38. Kleissl, J.; Meneveau, C.; Parlange, M.B. On the magnitude and variability of subgrid-scale eddy-diffusion coefficients in the atmospheric surface layer. *J. Atmos. Sci.* **2003**, *60*, 2372–2388. [CrossRef]
39. Kleissl, J.; Parlange, M.; Meneveau, C. Field experimental study of dynamic Smagorinsky models in the atmospheric surface layer. *J. Atmos. Sci.* **2004**, *61*, 2296–2307. [CrossRef]
40. Wyngaard, J.C. Toward numerical modeling in the Terra Incognita. *J. Atmos. Sci.* **2004**, *61*, 1816–1826. [CrossRef]
41. Chen, Q.; Tong, C. Investigation of the subgrid-scale stress and its production rate in a convective atmospheric boundary layer using measurement data. *J. Fluid Mech.* **2006**, *547*, 65–104. [CrossRef]
42. Hatlee, S.C.; Wyngaard, J.C. Improved subfilter-scale models from the HATS field data. *J. Atmos. Sci.* **2007**, *64*, 1694–1705. [CrossRef]
43. Chamecki, M.; van-Hout, R.; Meneveau, C.; Parlange, M.B. Concentration profiles of particles settling in the neutral and stratified atmospheric surface layer. *Bound.-Layer Meteorol.* **2007**, *125*, 25–38. [CrossRef]
44. Ramachandran, S.; Wyngaard, J.C. Subfilter-scale modelling using transport equations: Large-eddy simulation of the moderately convective atmospheric boundary layer. *Bound.-Layer Meteorol.* **2011**, *139*, 1–35. [CrossRef]
45. Higgins, C.W.; Meneveau, C.; Parlange, M.B. The effect of filter dimension on the subgrid-scale stress, heat flux, and tensor alignments in the atmospheric surface layer. *J. Atmos. Ocean. Technol.* **2007**, *24*, 360–375. [CrossRef]
46. Kumar, V.; Kleissl, J.; Meneveau, C.; Parlange, M.B. Large-eddy simulation of a diurnal cycle of the atmospheric boundary layer: Atmospheric stability and scaling issues. *Water Resour. Res.* **2006**, *42*, W06D09. [CrossRef]
47. Sullivan, P.P.; Edson, J.B.; Horst, T.W.; Wyngaard, J.C.; Kelly, M. Subfilter scale fluxes in the marine surface layer: Results from the Ocean Horizontal Array Turbulence Study (OHATS). In Proceedings of the 17th Symposium on Boundary Layer and Turbulence, American Meteorological Society, San Diego, CA, USA, 23 May 2006; Paper 4.1, pp. 1–8. Available online: http://ams.confex.com/ams/BLTAgFBioA/techprogram/paper_110884.htm (accessed on 7 June 2023).
48. Bou-Zeid, E.; Higgins, C.; Huwald, H.; Meneveau, C.; Parlange, M.B. Field study of the dynamics and modelling of subgrid-scale turbulence in a stable atmospheric surface layer over a glacier. *J. Fluid Mech.* **2010**, *665*, 480–515. [CrossRef]
49. Patton, E.G.; Horst, T.W.; Sullivan, P.P.; Lenschow, D.H.; Oncley, S.P.; Brown, W.O.J.; Burns, S.P.; Guenther, A.B.; Held, A.; Karl, T.; et al. The canopy horizontal array turbulence study. *Bull. Am. Meteorol. Soc.* **2011**, *92*, 593–611. [CrossRef]
50. Nguyen, K.X.; Horst, T.W.; Oncley, S.P.; Tong, C. Measurements of the budgets of the subgrid-scale stress and temperature flux in the convective atmospheric surface layer. *J. Fluid Mech.* **2013**, *729*, 388–422. [CrossRef]
51. Chow, F.K.; Moin, P. A further study of numerical errors in large-eddy simulations. *J. Comp. Phys.* **2003**, *184*, 366–380. [CrossRef]
52. Sullivan, P.P.; Patton, E.G. The effect of mesh resolution on convective boundary-layer statistics and structures generated by large-eddy simulation. *J. Atmos. Sci.* **2011**, *68*, 2395–2415. [CrossRef]
53. Geurts, B.J.; Fröhlich, J. A framework for predicting accuracy limitations in large-eddy simulation. *Phys. Fluids* **2002**, *14*, L41–L44. [CrossRef]
54. Sullivan, P.P.; Moeng, C.H.; Stevens, B.; Lenschow, D.H.; Mayor, S.D. Structure of the entrainment zone capping the convective atmospheric boundary layer. *J. Atmos. Sci.* **1998**, *55*, 3042–3064. [CrossRef]
55. Dai, Y.; Basu, S.; Maronga, B.; de Roode, S.R. Addressing the grid-size sensitivity issue in large-eddy simulations of stable boundary layers. *Bound.-Layer Meteorol.* **2021**, *178*, 63–89. [CrossRef]
56. Adrian, R.J. Stochastic estimation of the structure of turbulent fields. In *Eddy Structure Identification*; Bonnet, J.P., Ed.; Springer: Vienna, Austria, 1996; pp. 145–196. [CrossRef]
57. Kimura, Y.; Herring, J.R. Diffusion in stably stratified turbulence. *J. Fluid Mech.* **1996**, *328*, 253–269. [CrossRef]
58. Kaimal, J.C.; Finnigan, J.J. *Atmospheric Boundary Layer Flows*; Oxford University Press: New York, NY, USA, 1994. [CrossRef]
59. Bryan, G.H.; Morrison, H. Sensitivity of a simulated squall line to horizontal resolution and parameterization of microphysics. *Mon. Weather Rev.* **2012**, *140*, 202–225. [CrossRef]
60. Doubrawa, P.; Muñoz-Esparza, D. Simulating real atmospheric boundary layers at gray-zone resolutions: How do currently available turbulence parameterizations perform? *Atmosphere* **2020**, *11*, 345. [CrossRef]
61. Wyngaard, J.C. Changing the face of small-scale meteorology. In *Atmospheric Turbulence and Mesoscale Meteorology*; Federovich, E., Rotunno, R., Stevens, B., Eds.; Cambridge University Press: Cambridge, UK, 2004; pp. 17–34. [CrossRef]
62. Perot, J.B.; Gadebusch, J. A self adapting turbulence model for flow simulation at any mesh resolution. *Phys. Fluids* **2007**, *19*, 115105. [CrossRef]
63. Wyngaard, J.C.; Cóte, O.R.; Izumi, Y. Local free convection, similarity, and the budgets of shear stress and heat flux. *J. Atmos. Sci.* **1971**, *28*, 1171–1182. [CrossRef]
64. Moeng, C.H. A large-eddy simulation model for the study of planetary boundary-layer turbulence. *J. Atmos. Sci.* **1984**, *41*, 2052–2062. [CrossRef]
65. Moeng, C.H.; Wyngaard, J.C. Evaluation of turbulent transport and dissipation closures in second-order modeling. *J. Atmos. Sci.* **1989**, *46*, 2311–2330. [CrossRef]

66. Deardorff, J.W. Three-dimensional numerical modeling of the planetary boundary layer. In *Workshop on Micrometeorology*; Haugen, D.A., Ed.; American Meteorological Society: Boston, MA, USA, 1972; pp. 271–311.
67. Lumley, J.L. (Ed.) *Whither Turbulence? Turbulence at the Crossroads*; Springer: Berlin/Heidelberg, Germany, 1990; Volume 357. [CrossRef]
68. Leibovich, S.; Warhaft, Z. John Leask Lumley: Whither Turbulence? *Annu. Rev. Fluid Mech.* **2018**, *50*, 1–23. [CrossRef]
69. Goldstein, S. Fluid mechanics in the first half of this century. *Annu. Rev. Fluid Mech.* **1969**, *1*, 1–29. [CrossRef]